



AMERICAN METEOROLOGICAL SOCIETY

Weather and Forecasting

EARLY ONLINE RELEASE

This is a preliminary PDF of the author-produced manuscript that has been peer-reviewed and accepted for publication. Since it is being posted so soon after acceptance, it has not yet been copyedited, formatted, or processed by AMS Publications. This preliminary version of the manuscript may be downloaded, distributed, and cited, but please be aware that there will be visual differences and possibly some content differences between this version and the final published version.

The DOI for this manuscript is doi: 10.1175/WAF-D-16-0062.1

The final published version of this manuscript will replace the preliminary version at the above DOI once it is available.

If you would like to cite this EOR in a separate work, please use the following full citation:

Figuroa, S., J. Bonatti, P. Kubota, G. Grell, H. Morrison, S. Barros, J. Fernandez, E. Ramirez, L. Siqueira, G. Luzia, J. Silva, J. Silva, J. Pendharkar, V. Capistrano, D. Alvim, D. Enoré, F. Diniz, P. Satyamurty, I. Cavalcanti, P. Nobre, H. Barbosa, C. Mendes, and J. Panetta, 2016: The Brazilian Global Atmospheric Model (BAM). Performance for Tropical Rainfall forecasting and sensitivity to convective scheme and horizontal resolution. *Wea. Forecasting*. doi:10.1175/WAF-D-16-0062.1, in press.



1 **The Brazilian Global Atmospheric Model (BAM). Performance for Tropical Rainfall**
2 **forecasting and sensitivity to convective scheme and horizontal resolution**

3 Silvio N. Figueroa^{1,9}, José P. Bonatti¹, Paulo Y. Kubota^{1,9}, Georg A. Grell², Hugh Morrison³,
4 Saulo R. M. Barros⁴, Julio P. R. Fernandez¹, Enver Ramirez¹, Leo Siqueira⁵, Graziela Luzia¹,
5 Josiane Silva¹, Juliana R. Silva¹, Jayant Pendharkar^{1,9}, Vinicius B. Capistrano^{1,9}, Débora S.
6 Alvim^{1,9}, Diego P. Enoré¹, Fábio L. R. Diniz¹, Praki Satyamurti⁶, Iracema F.A. Cavalcanti¹,
7 Paulo Nobre^{1,9}, Henrique M. J. Barbosa⁷, Celso L. Mendes⁶ and Jairo Panetta⁸.

8
9 ¹ *Center for Weather Forecasting and Climate Studies/National Institute for Space Research,*
10 *Cachoeira Paulista, São Paulo, Brazil*

11 ² *Earth System Research Laboratory of the National Oceanic and Atmospheric Administration*
12 *(NOAA), Boulder, CO 80305, USA*

13 ³ *National Center for Atmospheric Research, 1850 Table Mesa Dr., Boulder, CO 80305, USA*

14 ⁴ *Department of Applied Mathematics, University of São Paulo, São Paulo, Brazil*

15 ⁵ *Rosenstiel School of Marine and Atmospheric Science, University of Miami, USA*

16 ⁶ *National Institute for Space Research, São José dos Campos, São Paulo, Brazil.*

17 ⁷ *Department of Physics, University of São Paulo, São Paulo, Brazil*

18 ⁸ *Technological Institute of Aeronautics (ITA), São José dos Campos, São Paulo, Brazil*

19 ⁹ *The Brazilian Research Network on Global Climate Change - Rede CLIMA, São José dos*
20 *Campos, São Paulo, Brazil*

21 *Submitted to Weather and Forecasting*
22 *(March 2016)*

23 **Corresponding author address:**

24 Silvio N. Figueroa
25 CPTEC/INPE, Rod Presidente Dutra, km 40, Cachoeira Paulista, São Paulo
26 CEP: 12.360-000, Brazil
27 E-mail: nilo.figueroa@inpe.br
28 Phone: 55-12-31868400, Fax: 55-12-3101-2835

29
30
31
32
33
34
35
36
37
38
39
40
41
42
43
44
45
46
47
48
49
50
51

ABSTRACT

This article describes the main features of the Brazilian Global Atmospheric Model (BAM), analyses of its performance for tropical rainfall forecasting, and its sensitivity to convective scheme and horizontal resolution. BAM is the new global atmospheric model of the Center for Weather Forecasting and Climate Research (CPTEC), which includes a new dynamical core and state-of-the-art parameterization schemes. BAM's dynamical core incorporates a monotonic two-time-level semi-Lagrangian scheme, which is carried out completely on the model grid for the tridimensional transport of moisture, microphysical prognostic variables, and tracers. The performance of the Quantitative Precipitation Forecast (QPF) from two convective schemes, Grell-Dévényi (GD) scheme and its modified version (GDM), and two different horizontal resolutions are evaluated against the daily TRMM Multi-satellite Precipitation Analysis over different tropical regions. Three main results are: a) the QPF skill was improved substantially with GDM in comparison to GD; b) the increase in the horizontal resolution without any ad-hoc tuning improves the variance of precipitation over continents with complex orography, such as Africa and South America, whereas over oceans there are no significant differences; and c) the systematic errors (dry or wet biases) remain virtually unchanged after 5 days forecast. Despite improvements in the tropical precipitation forecast, especially over southeastern Brazil, dry biases over the Amazon and La Plata remain in BAM. Improving the precipitation forecast over these regions remains a challenge for the future developments of the model to be used not only for Numerical Weather Prediction over South America but also for global climate simulations.

52 **1. Introduction**

53 Substantial progress has been made during the last decade in the development of Earth
54 System Models (ESMs) and simulation of many important features of the present global climate.
55 Nevertheless, most current models still have serious deficiencies in simulating the tropical
56 precipitation during the wet season over the Southern Hemisphere (December to February- DJF).
57 The largest errors are found over the six regions depicted in Fig.1a, which are: Central Africa,
58 Indian Ocean ITCZ (Intertropical Convergence Zone), South Pacific Convergence Zone (SPCZ),
59 Amazon Basin, South Atlantic Convergence Zone (SACZ), and La Plata Basin. For instance,
60 results from the Coupled Model Intercomparison Project phase 5 (CMIP5) show that most
61 models tend to underestimate rainfall over the Amazon Basin (e.g., Yin et al. 2013; Mehran et al.
62 2014; Gulizia et al. 2014) and exhibit persistent errors in simulating the South American
63 Monsoon System (SAMS) (Jones and Carvalho 2013). Over Africa and Australia, models also
64 show poor skill in precipitation simulation (Mehran et al. 2014) and the SPCZ is still poorly
65 simulated in CMIP5 models (Hirota and Takayabu 2013; Grose et al. 2014). Moreover, as
66 rainfall is a highly nonlinear phenomenon, it is difficult to trace-back the origin of errors by
67 using full Earth System Models.

68 Xie et al. (2012) and Ma et al. (2014) examined the correspondence between short- and
69 long-term systematic errors in atmospheric models and found that most of the systematic errors
70 in precipitation of climate simulations develop within the first few days (~5 days) of simulation.
71 Therefore, it is believed that improving quantitative precipitation forecasts (QPF) in short-time
72 integrations (1-7 days), for instance, may be useful for improving climate variability simulation.
73 With this perspective, the Brazilian Global Atmospheric Model (BAM) has been developed at
74 Center for Weather Forecasting and Climate Studies (CPTEC) of the National Institute for Space

75 Research (INPE) for use in time scales ranging from days to seasons and horizontal resolutions
76 $O(10-200\text{ km})$. The strategy was to develop a seamless framework for weather/climate
77 prediction. Hence, the same global atmospheric model used in deterministic NWP (1-10 days) or,
78 coupled to an ocean model, in probabilistic extended NWP (1-4 weeks) is designed to be used
79 also in a full ESMs (global coupled atmosphere-ocean-land-cryosphere) for seasonal climate
80 prediction and climate change studies.

81 A comprehensive performance analysis of the BAM model in NWP and climate
82 predictions is yet to be documented. The present work is focused on evaluating seven-day
83 tropical precipitation forecasts produced by BAM during the austral summer (DJF) of 2012/2013
84 over the Southern Hemisphere, against the daily Tropical Rainfall Measuring Mission (TRMM)
85 and Multi-satellite Precipitation Analysis (TMPA). The aim of this paper is to provide (a) a brief
86 description of the dynamical and physical processes in BAM; (b) a QPF skill evaluation of the
87 new model with two different convective parameterization schemes: the Grell and Dévényi
88 (2002, GD) ensemble scheme and its modified version (GDM) developed at CPTEC against the
89 TMPA data set; and (c) an evaluation of the impact of increased horizontal resolution (from 45 to
90 20 km) on the QPF skill. Although the importance of other physical processes such as radiation,
91 vertical diffusion, microphysics, and surface processes for tropical precipitation cannot be
92 overlooked, our main focus lie on deep convection, which is crucial for rainfall prediction
93 (Fritsch and Carbone 2004), and on the impact of increasing horizontal resolution on
94 precipitation forecasts.

95 Although this study evaluates the performance of the model over all the tropics, our main
96 attention lies over southeastern Brazil, where the maximum seasonal precipitation occurs during
97 DJF; and where large metropolitan areas (e.g., Sao Paulo, Rio de Janeiro and Belo Horizonte)

98 rely on precipitation for water supply and food production. Therefore, development of a stable
99 global atmospheric model and its validation are important for practical use in weather forecasting
100 over Brazil, as well as the atmospheric component of the Brazilian Earth System Model – BESM
101 (Nobre et al. 2013) for the seasonal climate prediction and climate change studies. Hence the
102 importance of this study is to identify strengths and weaknesses of BAM for its use as
103 operational NWP model and for further developments of the model. This paper is organized as
104 follows. In Section 2, the physics and dynamics formulations of the new model are briefly
105 described. Section 3 describes the design of the experiments; precipitation dataset and
106 methodology used. Evaluation of the QFP over the tropical region with two different convective
107 schemes and the evaluation of the impact of increased horizontal resolution on the QPF skill are
108 described in Section 4. Section 5 summarizes our results.

109

110 **2. Overview of model formulation**

111 The dynamical core and physics parameterizations in BAM are quite different from those
112 used in the previous CPTEC atmospheric global model (referred hereafter as AGCM3 or old
113 model). We describe here briefly the novelties and the motivations leading to the new model.
114 The original version of AGCM3 was adapted from the Center for Ocean–Land–Atmosphere
115 Studies (COLA) AGCM during the nineties (Cavalcanti et al. 2002). The evolution
116 CPTEC/COLA AGCM, which led to AGCM3 has been reported in, for example, Figueroa et al.
117 (2006), Panetta et al. (2007) and Barbosa et al. (2008) (see Table 1 for a summary). AGCM3 has
118 been extensively used in previous years for deterministic and probabilistic global operational
119 NWP (e.g., [Cunningham et al. 2014](#)), and has been coupled to an ocean model for seasonal
120 climate prediction and climate studies (e.g., Nobre et al. 2009; Nobre et al. 2013). Nevertheless,

121 many systematic errors in NWP and climate simulations were found for horizontal resolutions
122 $O(10-100\text{ km})$, such as an excess of oceanic tropical precipitation, wet biases over Andes and
123 spurious precipitation near the mountains at high latitudes, among others that will be shown later
124 in this article. These errors motivated the development of a new global atmospheric model,
125 which included a new dynamical core and state-of-the-art parameterization schemes.

126

127 *a. Dynamics core*

128 The dynamical core in BAM is a hydrostatic semi-implicit spectral model, based on a U-
129 V formulation, with a sigma/hybrid vertical coordinate, incorporating a monotonic two-time-
130 level semi-Lagrangian scheme for the tridimensional transport of moisture, microphysical and
131 tracers prognostic variables. This transport scheme, which can be used with both the Eulerian
132 and the semi-Lagrangian code options for the dynamics, is carried out on the model grid, with
133 moisture variables having no spectral representation. This dynamical core aims to be used for
134 weather and climate prediction at horizontal resolutions from 200 down to 10 km. In the next
135 subsections, some physical processes incorporated in BAM are described, with others are listed
136 in Tab.1. The documentation of the new model (dynamical core and physics formulations) will
137 be available as a technical report.

138

139 *b. Surface layer processes*

140 The land surface scheme is the Integrated Biosphere Simulator-IBIS version 2.6 (v.2.6)
141 of Foley et al. (1996) and Kucharik et al. (2000), which was improved at CPTEC by Kubota
142 (2012). This scheme is a dynamic global vegetation model, which represents a wide range of
143 processes, including land surface physics, canopy physiology, plant phenology, vegetation

144 dynamics and competition, and carbon and nutrient cycling. The evaluation studies of this
145 scheme over the Amazon (e.g., [Costa et al. 2007](#), [Costa and Piris, 2010](#)), and over the Brazilian
146 Northeast ([Cunha et al. 2013](#)) have shown the capability of this scheme well represents the
147 physical, physiological, and ecological processes occurring in vegetation and soils. Therefore,
148 this scheme coupled to the atmosphere is a useful tool for rainforest, land use, deforestation, and
149 climate change studies, especially over the Amazon.

150

151 *c. Cloud microphysics*

152 The double-moment bulk microphysics Morrison scheme ([Morrison et al. 2005](#), [Morrison](#)
153 [et al. 2009](#)) with predicted droplet concentration and coupling with the specified background
154 aerosol/cloud condensation nuclei (CCN) spectra is used. This scheme predicts the mass and
155 number mixing ratios of five hydrometeor categories (x): cloud droplets, rain, cloud ice, snow,
156 and graupel. The size distributions are represented by gamma functions: $N_x(D_x) =$
157 $N_{0x} D_x^{\mu_x} \exp(-\lambda_x D_x)$, where D_x is the particle diameter, and N_{0x} , λ_x , and μ_x are the intercept,
158 slope, and shape parameters of the size distribution respectively. The shape parameter is assumed
159 zero ($\mu_x=0$) for cloud ice and precipitation species. For cloud droplets, μ is calculated as a
160 function of the droplet number concentration following [Martin et al. \(1994\)](#). The slope and
161 intercept parameters are derived from the predicted mass (q_x) and number (N_x) mixing ratios and
162 specified μ_x . Equations for the time tendencies of q_x and N_x are similar to those in [Morrison et](#)
163 [al. \(2005\)](#), except for graupel, q_g and N_g are given by [Reisner et al. \(1998\)](#). This scheme is
164 coupled to the turbulent mixing scheme, which provides a sub-grid vertical velocity for droplet
165 activation and mixing of the cloud droplet and ice number mixing ratios, as well as to the
166 radiation scheme described in the next section using the predicted cloud droplet and ice effective

167 radii.

168

169 *d. Radiation and cloud properties*

170 The shortwave (SW) and longwave (LW) radiation scheme used in BAM is the Rapid
171 Radiative Transfer Model for GCMs (RRTMG, [Iacono et al. 2008](#)) developed at the
172 Atmospheric and Environmental Research, Inc. (AER), and which is a modified version of a
173 rapid and accurate radiate transfer model (RRTM, Mlawer et al. 1997). This scheme includes the
174 Monte-Carlo independent column approximation (McICA) technique ([Pincus et al. 2003](#)), which
175 is an efficient statistical method for sub-grid cloud characterization. The RRTMG-SW and
176 RRTMG-LW calculate fluxes and heating rates for the shortwave (14 bands, from 0.2 μm to
177 12.2 μm) and longwave (16 bands, from 3.1 μm to 1.0 mm) respectively. The effects of gaseous
178 absorption and particle scattering into RRTMG-SW include water vapor, carbon dioxide, ozone,
179 methane, oxygen, nitrogen, clouds, aerosols, and Rayleigh scattering, while the molecular
180 species treated into RRTMG-LW are water vapor, carbon dioxide, ozone, methane, nitrous
181 oxide, oxygen, nitrogen, and the halocarbons CFC11 and CFC12. On the other hand, the cloud
182 properties (cloud optical depth, emissivity, etc.) used in this new model are similar to those used
183 in the NCAR Community Atmosphere Model (CAM 5.0) described in Neale et al. (2012). The
184 aerosol optical properties are specified. The implementation of a dynamic aerosol model in BAM
185 is in progress, and is expected to be available in the next model version.

186

187 *e. Convection*

188 Shallow convection scheme in BAM is from Park and Bretherton (2009), which was
189 developed at University of Washington (UW). The cloud-base mass flux is calculated using

190 Turbulent Kinetic Energy (TKE) and Convection Inhibition Energy (CINE), and the entrainment
 191 and detrainment into cumulus updraft are calculated using a buoyance-sorting algorithm. Two
 192 deep convection schemes have been implemented in BAM. The multi-closure, Grell and
 193 Dévényi (2002) ensemble scheme (GD) and its modified scheme (GDM) developed at
 194 CPTEC/INPE (which is briefly summarized in Appendix). Below, we briefly describe the GD
 195 scheme focusing on the cloud-base mass flux.

196 Following Arakawa and Shubert (1974, hereafter AS) the cloud-work function (A) is the
 197 rate of generation of kinetic energy due to work done by buoyancy force (B), or an integral
 198 measure of the buoyance force with weighing by a normalized mass flux profile (η). The change
 199 of A can be written as $\frac{\partial A(t)}{\partial t} = \left(\frac{\partial A(t)}{\partial t}\right)_{LS} + \left(\frac{\partial A(t)}{\partial t}\right)_{CU} m_b$, where the subscripts LS and CU
 200 represent changes of the work function due to effects of the large-scale forcing (F), and due to
 201 the convective clouds (K) normalized by cloud base flux m_b , respectively. The Grell closure
 202 (Grell 1993, G1) assumes the AS convective quasi-equilibrium assumption between large-scale
 203 forcing and convection. This AS quasi-equilibrium assumption requires that $\frac{\partial A(t)}{\partial t} \ll F$. This
 204 means that convective tendencies are fast compared to the net or observed tendency, $\frac{\partial A(t)}{\partial t} \approx 0$,
 205 then the mass flux base m_b in G1 closure can be calculated as $m_b - F/K = -(A'(n+1) -$
 206 $A(n))/K\Delta t$, where A' is the work function calculated with updated (at time-step $n+1$)
 207 thermodynamics variables (ψ^{n+1}) after modifications by model tendencies (radiation, surface
 208 and PBL processes and dynamics) and A is calculated from thermodynamics variables at the
 209 present state (ψ^n) and K is calculated as in G1. The GD scheme implemented in BAM uses five
 210 different methods to calculate m_b . Three are stability closures. G1 (1) is described above. For AS
 211 (2), the closure from the GFS physics suite is used that uses climatological cloud work functions

212 instead of calculating A . KF-Type (3) removes stability over a specified time period (such is used
213 in Kain and Fritsch 1992). Kuo-type (4) uses a Krishnamurti type closure (Krishnamurti et al.
214 1983), relating the integrated vertical advection of moisture to m_b . The final closure (5) uses a
215 relationship between low level omega and m_b ([Brown 1979](#)). Three perturbations are then
216 applied for G1, FC_type, Kuo_type and omega, and four perturbation for AS. These are allowed
217 to interact with 9 members from static control (3 precipitation efficiencies and 3 cap strengths),
218 giving a total 144 sub-grid members.

219

220 **3. Experiments, data and methodology**

221 *a. Experimental design*

222 Four experiments have been performed. The first experiment (Exp1) uses AGCM3 and
223 the other three use BAM with two convective parameterizations, GD and GDM, which are
224 referred to as BAMA and BAMb respectively. Further details are given in Table 2. In the first
225 experiment, global precipitation from AGCM3 and BAM are compared (Section 4a). The QPF
226 evaluation over the tropics, sensitivity of precipitation forecast from the new model (BAM) with
227 two convective parameterizations (Exp2 and Exp3) and sensitivity to increasing the horizontal
228 resolutions (Exp4) are evaluated in two parts: Part 1 (Section 4b) - over the global tropics, SPCZ,
229 and over three land regions; and Part 2 (Section 4c) - over Brazil which was divided into 5
230 regions. The experiments at 20 km horizontal resolution were carried out with SL and Eulerian
231 advection schemes, but the results were similar (figures not shown). Therefore, we will focus
232 only on the SL results.

233 The period of simulation is from November 20, 2012 to February 28, 2013. This period
234 was chosen for the present study because during that specific period, i.e., austral summer, many

235 heavy rainfall events were observed. For instance, during DJF 2012/2013, 13 cold fronts over La
236 Plata, and 5 well-defined SACZ episodes occurred over southeastern Brazil (Climanálise 2012,
237 2013a and 2013b). Starting at every day in that period, the models were integrated for 7 days
238 using the same initial conditions used in the NCEP/GFS operational model, at 12 UTC. The 7-
239 days output total precipitation forecast was used for model evaluation. We use the initial
240 conditions from GFS to evaluate the performance of the new dynamic and physical processes
241 involved in BAM, rather than using our own assimilation system, to allow for a clear comparison
242 with precipitation forecast from GFS. In order to filter the spurious high-frequency oscillations
243 produced during the first time-steps of the forecast due to the unbalanced initial conditions, a
244 diabatic nonlinear normal-mode initialization (NNMI) scheme based on Machenhauer (1977)
245 and Kitade (1983) is used with the first five vertical modes, period cutoff of 48 h and two
246 interactions. In this scheme, the initial tendency of the faster modes is set to zero and the
247 corresponding fields of these waves are replaced by a new balanced fields obtained interactively.
248 This initialization process can alleviate the problem of surface pressure tendency spin-up during
249 the first few hours of integration.

250

251 *b. Data for QPF verification*

252 The daily observed rainfall for the tropical QPF evaluation is derived from TMPA
253 (Huffman et al. 2010) 3B42 version 7, 3-hourly $0.25^\circ \times 0.25^\circ$ lat/long grid resolution rainfall data
254 for the period December 2012-February 2013. Previous studies have evaluated the TMPA
255 product over different tropical regions, e.g., over Australia (Chen et al. 2013) and over the Andes
256 (Ochoa et al. 2014). These studies reveal that the TMPA product shows, in general, a good
257 correspondence with rain gauge data sets. In addition to TMPA, for evaluating the global

258 precipitation and surface latent heat fluxes for DJF 2012/2013, the daily Global Precipitation
259 Climatology Project (GPCP-v.2.2) $1^\circ \times 1^\circ$ lat/long grid ([Huffman et al. 2009](#)) product and the
260 European Centre for Medium-Range Weather Forecasts (ECMWF) Re-Analysis (ERA)-Interim
261 (ERA-Interim) product ([Dee et al. 2011](#)) are used, respectively. For comparison of QPF from
262 BAM and other global NWP operational models, 7-days precipitation forecast data from the
263 operational GFS (September 2012 version, horizontal resolution ≈ 27 km and 64 vertical levels)
264 is used, which are available on the NCEP website. Finally, the output precipitation data from all
265 experiments were gridded to the observed data resolution (e.g., tropical model precipitation to
266 the TMPA dataset resolution, 0.25° ; and global model precipitation to the GPCP dataset
267 resolution, 1°). For this interpolating, the *remapcon* utility from the CDO (Climate Data
268 Operators) package is used that performs first-order conservative remapping.

269

270 *d. Methodology and statistics*

271 For evaluating the QPF in each region we used standard continuous and categorical
272 statistical measures. The continuous statistics scores used to evaluate the accuracy of different
273 models are: unconditional bias (*BIAS*), root mean square error (*RMSE*), unbiased root mean
274 square error (*URMSE*), standard deviation (σ) and Pearson correlation coefficient (*R*). Following
275 Murphy (1988), the uncentered total RMSE can be decomposed in two components, due to the
276 systematic errors (*BIAS*) and related to the pattern error (*URMSE*). The *URMSE* (once the
277 unconditional biases are removed from the total error) can be interpreted as a measure of non-
278 systematic model errors due to errors in amplitude (σ) and phase (*R*). We use the Taylor (2001)
279 diagrams to graphically summarize the normalized unbiased RMSE (*URMSE**), the normalized
280 standard deviations forecast (σ_f^*) and the correlation coefficient (R_{fo}). This method is also used

281 to compare the performance of models to the observations.

282 The categorical forecast verification measures used here are: frequency bias score (*FBS*),
283 and the Gilbert skill score (*GSS*) also known as the Equitable Threat Score (*ETS*) (Mesinger and
284 Black 1992). The *FBS* and *GSS* are among the different categorical scores recommended by
285 WMO (2009) for assessing the skill of deterministic precipitation forecast. The threshold values
286 used for plots are similar to those used by Mesinger (1998) except in mm/day. Four different
287 rainfall categories, based on thresholds of precipitation intensity (in mm/day), are used in this
288 paper: very light rain (0.1-2.5), light rain (2.6-7.5), moderate rain (7.6-35.5) and heavy rain
289 (>35.6). These four rainfall categories have been adapted from the Indian Meteorology
290 Department-IDM glossary (http://www.imdpune.gov.in/weather_forecasting/glossary.pdf).

291

292 **4. Results**

293 *a. Global precipitation from AGCM3 and BAM*

294 In this section we evaluate the 24 h global DJF average precipitation and surface latent
295 heat fluxes from AGCM3, and BAM at 45 km horizontal resolution with two convective
296 parameterizations GD and GDM. Figure 1 shows the seasonal mean precipitation rate obtained
297 from GPCP and the 24 h model forecasts from the first three experiments (left) and the
298 corresponding surface latent heat fluxes (right). The comparison of surface latent fluxes is
299 included in this section, in order to identify the possible cause of the excessive tropical
300 precipitation in AGCM3. The spatially averaged RMSE and correlation coefficient values are
301 shown on the top right corners of the panels, and the zonal mean precipitation and surface latent
302 heat fluxes corresponding to Fig. 1 are shown in Fig. 2. An eyeball comparison of the results
303 from the old model (Fig. 1b) with the observations (Fig.1a) clearly shows large spurious

304 precipitation over the mountains in high latitudes (e.g., the Rocky, Himalayan, Greenland, and
305 Antarctic mountains), and large wet biases over the tropical region, especially over Africa, South
306 America, SPCZ, and ITCZs. Large differences over high and low latitudes between the old
307 model and GPCP can be vividly observed in Fig. 2a. These errors in AGCM3 are probably
308 caused by the horizontal diffusion applied to moisture and temperature computed in spectral
309 space along pressure surfaces. The new treatment of moisture in the new dynamic spectral core
310 of BAM with a semi-Lagrangian scheme for horizontal and vertical advection carried out
311 completely in grid-point space eliminated this problem (compare Fig.1c with Fig.1b over high
312 latitudes). In the new dynamical core, no horizontal diffusion is applied to
313 moisture, microphysics prognostic variables and trace constituents. In addition, the semi-
314 Lagrangian advection scheme employs a monotonic quasi-cubic interpolation method,
315 preventing the occurrence of over- or under-shootings. In particular, positive quantities remain
316 positive.

317 On the excessive ocean tropical precipitation present in the old model, which was
318 reduced drastically in BAMA, a comparison of the surface latent heat fluxes over tropical regions
319 (Fig. 1b') with Era-Interim (Fig. 1a') suggests that the origin of this wet bias is probably linked
320 to the errors in the surface fluxes formulation over the oceans. Although the forecast of global
321 precipitation in BAMA is improved (compare Fig. 1b with Fig. 1c, even more clearly in Fig. 2a)
322 wet biases still remain over the Pacific and Atlantic ITCZs, as well as over Africa and South
323 America. However, in BAMb (with GDM convective scheme), these errors are reduced
324 substantially (compare Figs. 1d and 1c), i.e., the wet biases over ITCZs, Africa, South America,
325 are largely reduced. On the other hand, while the surface latent heat fluxes do not change
326 significantly between BAMA and BAMb zonal averages, they do overcorrect for the excess

327 surface heat flux of AGCM3 (Fig. 2b). The precipitation patterns from 48 and 72 h forecast
328 (figures not shown) are similar to the ones in Fig.1 and 2. In brief, the GDM scheme in BAM
329 improved DJF global precipitation compared to the GD scheme and AGCM3, as can be clearly
330 seen in Fig. 2a, yet it is necessary to compare the daily forecast statistics from both convective
331 schemes for 7 day forecasts in order to conclude which convective scheme is better for QPF. In
332 the next sections we will not consider AGCM3 for the QPF evaluations anymore; instead, we
333 will mainly focus on the performance of BAM with two convective parameterizations (GD and
334 GDM) and two horizontal resolutions (45 and 20 km) against observations. Additionally, the
335 performance of BAM is compared with GFS results.

336

337 *b. Quantitative Precipitation Forecast over the Tropics*

338 In this section we focus on the QPF evaluation from Exp2 (45 km) and from Exp3 (45
339 km) and Exp4 (20 km) over the Tropics and GFS products against daily rainfall data from
340 TMPA. Initially, we analyze the first 24 h forecast mean precipitation (Fig. 3) by comparing the
341 output from BAMB at two horizontal resolutions and GFS against the observed precipitation
342 dataset to illustrate short-term precipitation forecast pattern over the Tropics. The left panel in
343 Fig. 3 shows that there are no substantial differences between BAMB at low (Fig. 3b) and high
344 (Fig. 3c) horizontal resolutions and GFS (Fig. 3d) (compare spatial root mean square and the
345 correlation coefficient values), and they appear quite similar to the observations (Fig. 3a).
346 However, in the right panel of Fig. 3, we can identify regions with dry and wet biases. The
347 similarity of dry and wet biases on all three panels on Figure 3' are noteworthy especially over
348 the mouth of the Amazon River, and southward anomalous displacement of the Atlantic ITCZ.
349 The main differences between BAMB at low and high resolutions (Figs. 3b' and 3c') are

350 observed over Africa and South America regions with complex topography, where the
351 precipitation forecasts are slightly increased at higher resolution (more details in Section 4c),
352 whereas over oceans there are no noticeable differences. In the case of GFS, major errors
353 (overestimation) are found over South America (e.g. the Andes), Central Africa and the tropical
354 and north Pacific Ocean, whereas minor errors are found over the maritime continent in
355 comparison to BAM with both resolutions. This visual evaluation over different tropical regions
356 will be analyzed later by their statistical metrics for the 7 days forecast, which will show that the
357 systematic errors over some regions observed in Fig. 3 for the 24 h forecast remain for the next
358 2-7 days forecast, and over other regions these errors change during 4' days forecast, but remain
359 virtually unchanged from 5 to 7 days forecast.

360 To analyze the QPF over the tropics, we have chosen 5 areas shown in Fig. 3a: global
361 Tropics (A1); three tropical continental areas: Africa (A2), northern Australia (A3) and South
362 America (A5); and SPCZ (A4). Figure 4 displays the time series of precipitation for models and
363 TMPA to illustrate the daily rainfall forecasts at lead times of 24 and 72 h, and Fig. 5 shows the
364 BIAS (left) and unbiased URMSE (right) for 1-7 days forecast. Figure 4a shows that the
365 precipitation amount over the global tropics for the 24 and 72 h forecast are overestimated by
366 BAMA and GFS whereas BAMb shows minor biases, which can be seen clearly in Fig. 5a. This
367 figure also shows that the precipitation bias observed during the first days remains similar for the
368 medium range forecast 5-7 days. The unbiased RMSE analyzed over the global tropics (Fig. 5a')
369 also shows minimum errors for BAMb compared to GFS and BAMA. The BIAS analysis in
370 specific regions shows (Fig. 4 and 5) that BAMA and GFS overestimate over Africa and South
371 America, while BAMb slightly underestimates precipitation. Over Australia and SPCZ the
372 precipitation biases undergo changes during the first 3 days forecast. Notwithstanding these

373 changes, the precipitation biases for 5 to 7 days forecast remain virtually unchanged (e.g., over
374 SPCZ) or they are enlarged (e.g., GFS and BAMb over Australia). In short, the systematic errors
375 from these models over tropical regions occur within the first five days of forecast. The unbiased
376 RMSE analyzed over different regions shows that BAMA has larger pattern errors than GFS and
377 BAMb.

378 The precipitation time series for BAMb at 20 km horizontal resolution (figure not shown)
379 are similar to that for BAMb at 45 km shown in Fig. 4, except over Africa and South America,
380 where the model at high-resolution increases the precipitation amount, shown in Fig. 5b and 5e.
381 However, there are no clear differences in RMSE at both resolutions. The average dry biases
382 over South America (Fig. 5e) are slightly improved at high horizontal resolution (more details in
383 Section 4c).

384 Figure 6 depicts the GSS along with the FBS of QPF with the 72 h forecasts from BAMA,
385 BAMb and GFS. The frequency bias score is useful to know whether the model overpredicted
386 ($FBS > 1$) or underpredicted ($FBS < 1$), i.e., indicating whether the model predicted either more
387 or fewer events than observed (it is different from the unconditional bias used before). A perfect
388 score of 1 means, that the forecast frequency is equal to the observed events regardless of
389 forecast accuracy. On the other hand, GSS is commonly used to evaluate the precipitation
390 forecast skill across different regimes, with GSS equal to 0 indicating no skill, 1 indicating a
391 perfect score and <0 a worse forecast than random. However, this score should be used in
392 combination with FBS (or by adjusting with bias score), because higher GSS scores can result
393 from FBS inflated beyond unity (Mesinger 2008). The analysis of FBS (Figs. 6a-e) and GSS
394 (Figs. 6a'-e') over the global tropics as well as over different tropical regions at low resolution
395 shows that BAMb performs much better than BAMA, with major skill improvement over SPCZ

396 for light and moderate rainfall. There are no significant differences in GSS scores over all
397 regions as the horizontal resolution is increased. However, a substantial improvement in FBS
398 (values near 1) with increased horizontal resolution for moderate and heavy rainfall over Africa
399 (Fig. 6b) and South America (Fig. 6e) is noted.

400 To further evaluate the models' performance for amplitude and phase of precipitation
401 patterns over the five areas of study, Taylor diagrams were computed and are shown in Fig. 7.
402 These diagrams allow for the intercomparison of unbiased RMSE, correlation coefficient, and
403 standard deviation for 1, 3, 5 and 7 days forecasts. In these diagrams, the radial distance (dotted
404 lines) from the origin to any given forecast point indicated by number (from 1 to 7 days forecast)
405 is the normalized standard deviations (σ_f^*), and their cosine of the azimuthal angle related to the
406 horizontal axis, gives the correlation coefficients (R_{fo}). The distance from the reference point
407 (black star) on the horizontal axis to any given forecast points is unbiased RMSEs ($URMSE^*$)
408 described in Section 3d. Fig. 7 shows, first, that BAMB performs better than BAMA over Africa,
409 Australia, South America and SPCZ in terms of RMSE, correlations and amplitude of spread
410 (standard deviation) with the lead time of 1 to 7 days consistent with the previous analyses.
411 Secondly, the results from BAMB at high resolution are similar to the results at low resolution,
412 except over Africa (Fig. 7b) and South America (Fig. 7e), where at 20 km an improvement in the
413 standard deviation is seen. These last results over Africa and South America are consistent with
414 FBS improvement over these regions, discussed later, and with the improvement in rainfall
415 intensity shown in Fig. 5. We speculate that this improvement, over regions with complex
416 terrain, can be attributed to improved representation of topographical forcing in high-resolution
417 models. It is interesting to see that over Australia and SPCZ, from Fig. 7c and 7d, errors increase
418 (and correlations diminish) as the lead time increases (in both resolutions and especially from 5

419 to 7 days). Although these results are obtained from an AGCM not coupled to an ocean model,
420 they also indicate that the precipitation predictability for medium range time scales in some
421 equatorial regions (e.g., Australia and SPCZ) can be higher than that at high latitudes, as has
422 been suggested by Stern (2011), Zhu et al. (2014) and Stern and Davidson (2015).

423 In summary, the QPF evaluation from different versions of BAM shows that BAMb at 45
424 km gives better performance than BAMa (in terms of FBS, GSS, RMSE, BIAS, standard
425 deviation and correlations) over all tropical regions analyzed here. On the other hand, the bias
426 scores of moderate and heavy rain (both intensity and standard deviation) are improved at high-
427 resolution over Africa and South America, which indicate the importance of resolution to
428 improve the representation of extreme precipitation events over these regions. An additional
429 result is that systematic errors (bias) in the model over tropical regions occur within the first 5
430 days of forecast.

431 *c. Quantitative Precipitation Forecast over Brazil*

432 To evaluate the performance of BAM for QPF over Brazil up to 7 days, we have chosen 5
433 regions covering the country, namely, B1, B2, B3, B4 and B5 shown in Fig. 8. Region B5
434 includes northern Brazil where the Brazilian Amazon basin (hereafter called Amazon) is located;
435 region B4 includes most of northeastern Brazil (referred here as Northeast); region B3 includes
436 central-west Brazil, eastern Bolivia and northern Paraguay (Central-West); region B2 includes
437 most of southeastern Brazil and surrounding oceanic areas (referred here as Southeast), where
438 the large Brazilian cities are located (e.g., Rio de Janeiro, São Paulo and Belo Horizonte); and B1
439 represents approximately the La Plata Basin, which includes most of southern Brazil, Uruguay,
440 northeastern Argentina, and southern Paraguay (hereafter called La Plata).

441 Before analyzing the QPF from BAMb, we will review briefly the main features that

442 affect the daily precipitation over regions B1 to B5 focusing on the period DJF 2012/13. Fig. 9
443 shows the time series of precipitation for the models and TMPA to illustrate the models' daily
444 precipitation forecast for 24 h (left) and 72 h (right) over the regions defined in Fig. 8 in
445 comparison to observations.

446 The systems that affect the daily precipitation over La Plata region during DJF are frontal
447 systems (Garreaud and Wallace 1998), mesoscale convective systems (MCSs) and
448 cyclogenesis (e.g., Salio et al. 2007, Romatschke and Houze 2010, Boers et al. 2015, Rasmussen
449 et al. 2016). The La Plata basin is a preferred region over southern South America for tropical-
450 extratropical interactions between the large-scale synoptic baroclinic waves (upper-level jet
451 streams and their associated fronts) and warm and moist low-level advection by the low-level jet
452 (LLJ) on the eastern side of the Andes from the Amazon region, generating the majority of
453 MCSs observed in this region (e.g., Berbery and Barros 2002, Salio et al. 2007, Rozante and
454 Cavalcante 2008, Arraut and Barbosa 2009, Arraut and Satyamurty 2009, Boers et al., 2014,
455 Rasmussen and Houze 2016). Although the occurrence of some MCSs over this region do not
456 relate to the frontal systems, the most numerous and intense MCSs tend to occur in connection
457 with LLJ and cold fronts passing over the southern Andes and arriving to the northern Argentina,
458 Uruguay and Southern Brazil (Romatschke and Houze 2010, Rasmussen and Houze 2016).

459 During DJF 2012/2013, 13 cold fronts were identified over the region (Climanálise,
460 2012, 2013a, and 2013b), which is indicated by letter *F* in Fig. 9a (from to F_1 to F_{13}), giving an
461 average of a cold front passage every 7 days. We can see that all models forecasted these systems
462 24 and 48 h in advance, although with different intensities.

463 Among the main systems that produce rainfall over the Southeast (B2) (e.g. the SACZ,
464 frontal systems, MCSs, squall lines; and land-sea breeze circulation), the SACZ (a quasi-

465 stationary meteorological perturbation that lasts for 3 to 7 days, approximately) is the most
466 important synoptic systems directly affecting the Region. In addition, this system indirectly
467 affects the weather conditions over South, Central-West, North, and Northeast regions of Brazil
468 during DJF (Nogués-Peagle and Mo (1997)). SACZ's origin is not fully understood. However,
469 preliminary modeling studies suggest that interaction between intense convection over the
470 Amazon (as local forcing) with large-scale westerly winds (e.g., Figueroa et al. 1995) or frontal
471 system (e.g., Ferreira, et al. 2013) could be a possible cause of SACZ initiation. The dynamics of
472 enhanced cloudiness and rainfall over cooler SST associated to the SACZ could be better
473 explained by the use of coupled ocean-atmosphere models and direct observations (e.g., De
474 Almeida et al. 2007).

475 Despite this fact, the 5 SACZ episodes identified during DJF 2012/2013 (Climanálise,
476 2012, 2013a and 2013b), indicated by the letter *S* in Fig. 9b (from S_1 to S_5) were well predicted
477 by BAMb as well as GFS, both their duration and intensity, 24 and 72-h in advance. Only in the
478 S_4 event, at the end of January (around day 60), precipitation amount was underestimated by
479 BAMb. A comparison of Fig. 9a and 9b shows an alternation between the extreme precipitation
480 events over the SACZ and La Plata regions, which is known as the South American dipole
481 (Nogués-Paele and Mo, 1997).

482 When intense and persistent SACZ events occur over Southeast (e.g. during January
483 2013, days 32-63), the precipitation over the La Plata region is drastically reduced. Conversely,
484 when persistent intense precipitation occurs over La Plata (e.g., in December, days 1-31), the
485 development of intense SACZ events are inhibited. This dipole-like precipitation structure on
486 intraseasonal time scales between La Plata and southeastern Brazil, identified in many
487 observational studies (e.g., Nogués-Paele and Mo, 1997), were reproduced well by the BAMb

488 and GFS models, but overestimated by BAMA. While SACZ is a quasi-stationary system, the
489 cold fronts arriving in this region from southern Brazil are transient perturbations, and the
490 convective bands associated with them rapidly move northeastward (Lima et al. 2009). Most of
491 the intense MCSs over this region are linked to these frontal incursions (Siqueira and Marques,
492 2010). Also, these transient systems are responsible for maintaining or intensifying the
493 convective activity in the SACZ driving extreme precipitation events over this region.

494 Weather conditions over Central-West region (B3) are also affected by squall lines,
495 MCSs, SACZ (mainly over the eastern part of this region) and frontal systems that occasionally
496 reach the southern part of this region. The maximum seasonal precipitation over the Northeast
497 (B4) occurs during March-April-May (MAM), and is linked to the Atlantic ITCZ southernmost
498 annual displacement (Moura and Shukla 1981; Nobre and Shukla 1996). However, weather
499 conditions during DJF over the southern Northeast are affected by convective activity associated
500 with the upper-level cyclonic vortices, easterly waves, land-sea breeze circulation (over coastal
501 regions of B4), as well as occasional cold fronts and SACZ reaching the southern part of this
502 region (Chaves and Cavalcanti 2001). For instance, intense precipitation during the last 15 days
503 of January (days 45-60) over the Northeast (Fig. 10d) was related to SACZ events (compare Fig.
504 9d with Fig. 9b). Finally, weather conditions over the Amazon (area B5) during DJF are affected
505 by convection organized by SACZ (Vieira et al. 2012), MCSs, and squall lines, which originate
506 on the northern coast of Brazil and propagate toward the Amazon, although these systems are
507 more frequent during MAM (Cohen et al. 1995). The time series of TMPA precipitation
508 estimated over the Amazon (Fig. 9e) shows a large rainfall variability during the intense SACZ
509 events over Southeast (days 45 to 75), although the maximum precipitation values over Amazon
510 and SACZ regions do not occur simultaneously.

511 Similar to Figure 4 (left), Figure 10 (left) shows that the tendencies of the systematic
512 errors (e.g., dry bias over the Amazon and La Plata) remain unchanged from 5 to 7-days forecast.
513 The RMSE (Fig. 10, right panel) shows that BAMB (at both 45 and 20 km resolution) performs
514 much better than BAMA. Figure 11 depicts the GSS (right) along with FBS (left) at 72-h lead
515 time for the areas defined in Fig. 8. A visual inspection of the frequency bias (Fig.11a-e) shows
516 that BAMA overpredicts moderate and heavy rainfall events over all regions, except over the
517 Amazon, whereas BAMB at 45 km underpredicts. However, it is improved (FBS values near 1)
518 at high resolution, mainly over the Southeast. The GSS analysis shows that BAMB at 45 km is
519 superior to BAMA for light and moderate rainfall over the Southeast and La Plata, whereas over
520 other regions there are not clear differences. Over La Plata Fig. 11a and a), GFS performs much
521 better than BAMB in terms of GSS, however in FBS analysis all models overpredict of
522 occurrence of light and moderate rainfall. Major improvement of BAMB (FBS and GSS) at high
523 resolution for moderate and heavy rainfall compared to BAMA at 45 km is found over the
524 Southeast (Fig. 11b, Fig. 11b'), even beyond 72 h forecast (not shown). On the other hand, over
525 the Amazon all models display lower Gilbert skill score (Fig. 11e'). Improvement in QPF skill
526 over this region will remain a great challenge.

527 A comparison of precipitation forecast statistics using the Taylor diagram (Fig. 12) and
528 Biases (Fig.11, left) shows that BAMB is generally superior to BAMA for 1 to 7 day lead time
529 forecasts (smaller URMSE*, higher correlations and smaller BIAS), except over the Amazon and
530 La Plata; where they have similar performance. On the other hand, the comparisons between
531 GFS and BAMB for 1 to 7 day forecasts at 45 km show similar URMSE* and correlations over
532 La Plata, Southeast, Central-West and Northeast, notwithstanding the magnitude of the daily
533 variability is better forecast by GFS. The performance of BAMB at high-resolution is similar to

534 that at 45 km, except over the Southeast (B2) and Central-West (B3) (compare red and black
535 color numbers in Fig. 12). Over these regions, one can see the improvement of the spread
536 (standard deviation) of precipitation at high-resolution, which is more noticeable over Southeast.
537 These results are consistent with the improvements in precipitation intensity, frequency bias and
538 Gilbert skill score for moderate and heavy rainfall over Southeast as discussed before.

539 In summary, the version of BAM with the GDM scheme outperforms the model with the
540 GD scheme for QPF over the regions depicted in Fig 8. A comparison of results from low and
541 high horizontal resolutions shows that the frequency bias as well as the Gilbert skill score are
542 improved for moderate and heavy rainfall over the Southeast as the horizontal resolution
543 increases (Fig. 11b and 11b'). The variance of precipitation over the Southeast also improves at
544 high horizontal resolution (Fig.12d). Finally, the systematic forecast errors in precipitation (dry
545 or wet biases) over the regions shown in Fig. 8 remain practically unchanged from 5 to 7 days
546 forecast.

547

548 **5. Summary and conclusions**

549 The Brazilian Global Atmospheric Model (BAM) has been developed to overcome a
550 number of shortcomings present in the previous CPTEC atmospheric global model (AGCM3) for
551 the use over time scales ranging from days to seasons and horizontal resolution $O(10-100\text{ km})$.
552 BAM's dynamical core incorporates a monotonic two-time-level semi-Lagrangian scheme for the
553 transport of moisture and microphysics prognostic variables, and tracers, which are carried out
554 completely on the model grid space. Some state-of-art physical parameterization schemes
555 included in BAM are two convective parameterization schemes: GD and GDM, among the
556 others (listed in Table 1).

557 The QPF skill from BAM with GD and GDM schemes and sensitivity to increasing the
558 horizontal resolutions are evaluated against the daily TRMM Multi-satellite Precipitation
559 Analysis (TMPA) over the tropical region for up to seven days lead time during austral summer
560 2012/2013. Three main results are summarized here: a) the QPF skill was improved substantially
561 with GDM in comparison to GD (smaller biases, smaller unbiased RMSE, higher correlations,
562 improved frequency bias score-FBS and Gilbert skill score-GSS) over all tropical regions
563 evaluated (defined in Fig. 3a and Fig. 8); (b) the increase in horizontal resolution from 45 to 20
564 km, without any ad-hoc tuning, enhances the intensity and variance of precipitation, and
565 improves the frequency statistics of moderate and heavy rainfall events over the tropical
566 continents with complex orography, such as Africa and South America, mainly over southeastern
567 Brazil. Nevertheless, there was little difference between low and high resolutions over the
568 oceans; and (c) the systematic errors (dry or wet biases) seen during the first-day forecast over
569 some tropical regions remained similar or increased with time (e.g., Central Africa, Amazon, La
570 Plata), whereas in other regions there were changes during the first 1-4 days forecast. However,
571 these errors remain virtually unchanged after 5 days forecast.

572 From the first result stated above, we conclude that improving the convective
573 parameterization in BAM (for which the Single- Column Model and Cloud Resolving Model
574 were useful tools) is a key to improving the QPF over the tropics. From the second result, we
575 conclude that increasing the horizontal resolution in BAM from 45 to 20 km can benefit
576 operational NWP over tropical continents with complex topography for predicting extreme
577 rainfall events (e.g. during the SACZ events), mainly over Southeastern Brazil.

578 Two caveats to this evaluation are pointed out. (a) The quality of forecast from BAM can
579 be affected by the use of initial conditions produced from other data assimilation systems (i.e.,

580 NCEP/GFS). However, using the same initial condition as the NCEP/GFS forecast system has
581 made the model comparison more robust. (b) The period of evaluation, 7 days forecast for 3
582 months might not be enough for drawing conclusions regarding the performance of the new
583 model for precipitation forecast. Further, QPF and other variables (e.g., wind, temperature,
584 radiation, clouds, etc.) evaluation for different seasons of the year and for different years using
585 CPTEC's data assimilation system is necessary. Yet, the present exercise served to show relevant
586 improvements of precipitation forecast by the new convective scheme GDM compared to the
587 original GD scheme, as well as to explore the benefits of using 20 km horizontal resolution of
588 CPTEC global model in operational NWP. Based in this study, the semi-Lagrangian TQ666L96
589 (≈ 20 km and 96 vertical levels) BAM has become operational on January 01, 2016, (after being
590 used in experimental mode for one year), replacing the previous operational TQ299L64 (\approx
591 45 km and 64 vertical levels).

592 Although tropical precipitation forecasts have been improved with BAM, especially over
593 the southeast of Brazil, the total rainfall and its variance over the Amazon and La Plata regions
594 are still underestimated. In the next paper, we will show that similar systematic errors are found
595 in BAM climate simulations with prescribed sea surface temperature. Improving the precipitation
596 forecast over these regions remains a challenge for the future BAM developments.

597 *Acknowledgements*

598 The authors acknowledge NCEP for providing the analysis data set used in this study as well as
599 forecasts of NCEP/GFS. The authors thank Dr. Fedor Mesinger and the reviewers for a critical
600 review of this manuscript and constructive comments. This research was partially funded by the
601 Brazilian agencies: FAPESP, CNPq and the Brazilian Research Network on Global Climate
602 Change FINEP/Rede CLIMA, Grant Number 01.13.0353-00.

APPENDIX

The modified Grell and Dévényi convective scheme (GDM)

We have found in our experiments that by using GD scheme in BAM (either ensemble and individual closures), the rainfall over ITCZs, Africa and South America, mainly over the Andes are systematically overestimated (Fig.1c) which is discussed in Section 3. The large wet biases over the Andes have been investigated using BAM Single-Column Model (BAM-SCM) and the System of Atmospheric Modeling (SAM, Version 6.8.2) Cloud Resolving Model (CRM) developed by Khairoutdinov and Randall (2003). Based on these results, the original GD scheme described above was modified considering two important aspects: 1) AS, KF_type , Kuo_type and Omega closures were excluded and instead an undiluted CAPE (convective available potential energy)-based closure described in Zhang (2002) and Zhang (2009) was included; and 2) the original entrainment rate scheme ($\varepsilon = \frac{0.2}{R}$) was replaced by a new simplified scheme ($\varepsilon = \frac{\varepsilon_0}{z(k) - z(kb-1)}$), where R is the radius of the rising plume (12000 m), $z(k)$ is the height at model level k , $z(kb)$ is the height at cloud base level ($z(k) > z(kb - 1)$), and ε_0 a tunable parameter of $O(10^{-2})$. In Table A1, we summarized the closures and parameters used in this scheme, which is referred here as GD modified (GDM) scheme. Its performance in global NWP compared to GD scheme (e.g., Fig.1d and Fig.1c) is discussed in Section 4. The details of this modified scheme, and its impact on the improvement of precipitation simulation over the Andes will be reported in a separate article (paper in preparation). The remainder of this section describes how GD scheme was modified using SAM and BAM-SCM, and the main reason for the improvement of the simulated precipitation over the Andes with the modified scheme.

The averaged large-scale forcing (temperature and humidity advections, pressure, wind and vertical velocity) used for the CRM (1 km \times 1 km horizontal grid spacing, 144 \times 144 grid

626 points and with the two-moment Morrison microphysics scheme, Morrison et al. 2009) and SCM
627 simulations (BAM-SCM with parameterization physics described in Table 1), were calculated
628 from the 6 hourly NCEP/GFS analysis for the period 01 to 30 January 2013, over an $5^\circ \times 5^\circ$
629 (latitude-longitude) area centered approximately over the Peru-Bolivian Plateau (16.5° S - 69°
630 W). First, the precipitation from CRM was compared with the daily precipitation estimated by
631 satellite (TMPA, database details in Section 3) then results from BAM-SCM were compared
632 with the CRM simulations.

633 The CRM simulates the precipitation reasonably well in comparison to TMPA with
634 maximum values around 10 mm/day, although uncertainties exist in precipitation and large-scale
635 forcing estimated over complex topography. The results from BAM-SCM show (figure not
636 shown) that the daily precipitation patterns and intensity are poorly simulated when using the
637 original GD scheme in comparison to CRM and observations, in contrast results from GDM are
638 similar to CRM. Overall the GD scheme overestimates TMPA by approximately three-fold. We
639 found that results were much improved when we only used G1 and Zhang as closures, so all
640 other closures were excluded in GDM. The averaged (January 2013) mass-flux profile from
641 CRM/SAM, BAM-SCM with the GD scheme and 1D with the GDM scheme shows (figure not
642 shown) that the mass-flux from GD is almost three times higher than from CRM (maximum
643 value from CRM is around $0.02 \text{ kg/m}^2/\text{s}^2$), whereas that from GDM, at least in the first 6 km
644 above cloud-base, is close to the CRM results. The improvement in GDM simulation is attributed
645 mainly to: a) the exclusion of some closures b) addition of the CAPE-based closure and; c)
646 inclusion of the new simple entrainment scheme with ϵ_0 tuned using CRM/SAM results.

647

648 **References**

649 Alpert, J. C., M. Kanamitsu, P. M. Caplan, J. G. Sela, G. H. White, and E. Kalnay, 1988:
650 Mountain induced gravity wave drag parameterization in the NMC medium-range model.
651 Preprints of the Eighth Conference on Numerical Weather Prediction, Baltimore, MD,
652 AMS, 726-733.

653 [Arakawa, A., and W. H. Schubert, 1974: Interaction of a cumulus cloud ensemble with the large-](#)
654 [scale environment, Part I, J. Atmos. Sci. **31** 674–701.](#)

655 Arraut, J. M., H. M. J. Barbosa, 2009: Large Scale Features Associated with Strong
656 Frontogenesis in Equivalent Potential Temperature in the South American Subtropics East
657 of the Andes. *Adv. in Geosciences*, **22**, 73-78.

658 ———, J. M., P. Satyamurty, 2009: Precipitation and water vapor transport in the Southern
659 Hemisphere with emphasis on the South American region. *J. Appl. Meteorol. Climatol.*,
660 **48**, 1902-1912.

661 Barbosa, H. M. J., T. A. Tarasova and I. F. A. Cavalcanti, 2008: Impacts of a New Solar
662 Radiation Parameterization on the CPTEC AGCM Climatological Features. *J. Appl.*
663 *Meteorol. Climatol.*, **47**, p1377-1392.

664 [Berbery, E. H., and V. R. Barros, 2002: The hydrologic cycle of the La Plata basin in South](#)
665 [America *J. Hydrometeorol.*, **3**, 630-645.](#)

666 Boers, N., B. Bookhagen, H. M. J. Barbosa, N. Marwan, J. Kurths, and J. Marengo, 2014:
667 Prediction of Extreme Floods in the Eastern Central Andes based on a Complex Network
668 Approach. *Nature Communications*, **5**, 5199.

669 —, N., H. M. J. Barbosa, B. Bookhagen, J. A. Marengo, N. Marwan and J. Kurths, 2015:
670 Propagation of Strong Rainfall Events from Southeastern South America to the Central
671 Andes. *J. Climate*, **28**, 7641–7658.

672 Brown, J. M., 1979: Mesoscale unsaturated downdrafts driven by rainfall evaporation: A
673 numerical study. *J. Atmos. Sci.*, 36, 313–338, 1979.

674 Cavalcanti, I. F. A., and coauthors 2002: Global climatological features in a simulation using the
675 CPTEC-COLA AGCM. *J. Climatol.*, **21**, 2965-2988.

676 Chaves, R. R., and I. F. A. Cavalcanti, 2001: Atmospheric Circulation Features Associated with
677 Rainfall Variability over Southern Northeast Brazil. *Mon. Weather Rev.*, **129**, 2614–2626.

678 Chen, Y., E. E. Ebert, K. J. E. Walsh and N.E. Davidson, 2013: Evaluation of TMPA 3B42 daily
679 precipitation estimates of tropical cyclone rainfall over Australia. *J. Geophys. Res.*, **118**, 1-
680 13.

681 Chou, M. D., and M. J. Suarez, 1999: A solar radiation parameterization for atmospheric studies.
682 *NASA Tech. Rep. NASA/TM-1999-10460*, vol. **15**, 40 pp.

683 Climanálise, 2012: *Boletim de monitoramento e análise climática*, **27**, No12.
684 <http://climanalise.cptec.inpe.br/~rclimanl/boletim/pdf/pdf12/dez12.pdf>

685 —, 2013a: *Boletim de monitoramento e análise climática*, **28**, No1.
686 <http://climanalise.cptec.inpe.br/~rclimanl/boletim/pdf/pdf13/jan13.pdf>

687 —, 2013b: *Boletim de monitoramento e análise climática*, **28**, No2.
688 <http://climanalise.cptec.inpe.br/~rclimanl/boletim/pdf/pdf13/fev13.pdf>

689 Cohen, J. C. P, M. A. F. Silva Dias, and C. A. Nobre, 1995: Environmental Conditions
690 Associated with Amazonian Squall Lines: A Case Study. *Mon. Wea. Rev.*, **123**, 3163–
691 3174.

692 [Costa, M. H., S. N. M. Yanagi, P. J. Oliveira, A. Ribeiro and E. J. P. Rocha, 2007: Climate](#)
693 [change in Amazonia caused by soybean cropland expansion, as compared to caused by](#)
694 [pasture land expansion. *Geophysical Research Letters*, **34**: L07706, DOI:](#)
695 [10.1029/2007GL029271.](#)

696 [Costa, M. H. and G. F. Pires, 2010: Effects of Amazon and Central Brazil deforestation scenarios](#)
697 [on the duration of the dry season in the arc of deforestation, *Int. J. Climatol.*, **30**, 1970–](#)
698 [1979.](#)

699 Cunha, A.P.M.A, R.C.S Avalá, G. Sampaio, M.H. Shimizu and M. H. Costa, 2013: Calibration
700 and Validation of the Integrated Biosphere Simulator (IBIS) for a Brazilian Semiarid
701 Region. *J. Appl. Meteor. Climatol.*, **52**, 2753–2770.

702 [Cunningham, C., Bonatti, J. P. and Ferreira, M. \(2014\), Assessing improved CPTEC](#)
703 [probabilistic forecasts on medium-range timescale. *Meteorol. Appl.* doi: 10.1002/met.1464](#)

704 [Dee, D. P., and coauthors, 2011: The ERA-Interim reanalysis: configuration and performance of](#)
705 [the data assimilation system. *Quart. J. Roy. Meteorol. Soc.*, **137**, 553–597.](#)

706 [De Almeida, R. a. F., P. Nobre, R. J. Haarsma, and E. J. D. Campos, 2007: Negative ocean-](#)
707 [atmosphere feedback in the South Atlantic Convergence Zone. *Geophys. Res. Lett.*, **34**,](#)
708 [L18809.](#)

709 [Ferreira R.N. and W.C. Chao, 2013: Aqua-planet simulations of the formation of South Atlantic](#)
710 [convergence zone. *Int. J. Climatol*, **33**: 615–628 \(2013\).](#)

711 Figueroa, S. N., T. Tarasova, H. M. J. Barbosa, J. P. Bonatti, and P. L. Silvia Dias, 2006: The

712 impact of cumulus and radiation parameterization schemes on Southern Hemisphere
713 summer climate simulated by CPTEC atmospheric general circulation model. Proc. Eighth
714 Int. Conf. on Southern Hemisphere Meteorology and Oceanography, Foz do Iguacu,
715 Brazil, 1037-1040.

716 —, P. Satyamurty, and P. L. Silva Dias, 1995: Simulations of the summer circulation over the
717 South American region with an ETA coordinate model. *J. Atmos. Sci.*, **52** 1573-1584.

718 Foley, J. A., I. C. Prentice, N. Ramankutty, S. Levis, D. Pollard, S. Sitch, and A. Haxeltine,
719 1996: An integrated biosphere model of land surface processes, terrestrial carbon balance,
720 and vegetation dynamics. *Global Biogeochem. Cycles*, **10**, 603–628.

721 Fritsch, J.M. and R.E. Carbone, 2004: Improving Quantitative Precipitation Forecasts in the
722 Warm Season: A USWRP Research and Development Strategy. *Bull. Amer. Meteorol.*
723 *Soc.*, **85**, 955–965.

724 [Garreaud, R. D. and J. M. Wallace, 1998: Summertime incursions of midlatitude air into](#)
725 [subtropical and tropical South America. *Mon. Wea. Rev.*, **126**, 2713–2733.](#)

726 [Grell, G., 1993: Prognostic evaluation of assumptions used by cumulus parameterizations, *Mon.*](#)
727 [*Wea. Rev.*, **121**, 764– 787.](#)

728 —, and D. Dévényi, 2002: [A generalized approach to parameterizing convection combining](#)
729 [ensemble and data assimilation techniques, *Geophys. Res. Lett.*, **29**, 38-1-38-4,](#)
730 [DOI: 10.1029/2002GL015311](#)

731 Grose, M. R. and coauthors, 2014: Assessment of the CMIP5 global climate model simulations
732 of the western tropical Pacific climate system and comparison to CMIP3. *Int. J. Climatol.*,
733 doi: 10.1002/joc.3916.

734 Gulizia, C. and I. Camilloni, 2014: Comparative analysis of the ability of a set of CMIP3 and

735 CMIP5 global climate models to represent precipitation in South America. *Int. J. Climatol.*,
736 doi: 10.1002/joc.4005.

737 [Hirota, N. and Y. N. Takayabu, 2013: Reproducibility of precipitation distribution over the](#)
738 [tropical oceans in CMIP5 multi-climate models compared to CMIP3. *Clim. Dyn.*, **41**,](#)
739 [2909–2920.](#)

740 [Holtslag, A. A. M., and B. A. Boville, 1993: Local versus nonlocal boundary-layer diffusion in a](#)
741 [global climate model. *J. Climate*, **6**, 1825–1842.](#)

742 [Huffman, G. J., R. F. Adler, D. T. Bolvin, and G. Gu, 2009: Improving the global precipitation](#)
743 [record: GPCP version 2.1. *Geophys. Res. Lett.*,**36**, L17808, doi:10.1029/2009GL040000.](#)

744 Huffman, G. J., R. F. Adler, D. T. Bolvin, E. J. Nelkin, 2010: The TRMM Multi-satellite
745 Precipitation Analysis (TMPA), in: Satellite Applications for Surface Hydrology, edited
746 by: Gebremichael, M. and Hossain, F., Springer Science, New York, USA.

747 [Iacono, M., J. Delamere, E. Mlawer, M. Shephard, S. Clough, and W. Collins, 2008: Radiative](#)
748 [forcing by long-lived greenhouse gases: Calculations with the AER radiative transfer](#)
749 [models. *J. Geophys. Res.*, **113**, D13103, doi:10.1029/2008JD009944.](#)

750 Jones, C., and L. M. V. Carvalho, 2013. Climate change in the South American Monsoon
751 System: Present climate and CMIP5 projections. *J. Climate*, **26**: 6660-6678.

752 [Kain, J.S., and J.M. Fritsch, 1992:The role of the convective “trigger function” in numerical](#)
753 [forecasts of mesoscale convective systems. *Meteorol. Atmos. Phys.*, **49**, 93–106, 1992.](#)

754 [Khairoutdinov, M. F., and D.A. Randall, 2003: Cloud-resolving modeling of the ARM summer](#)
755 [1997 IOP: Model formulation, results, uncertainties and sensitivities. *J. Atmos. Sci.*, **60**,](#)
756 [607-625.](#)

757 [Kitade, T., 1983: Non-linear normal mode initialization with physics, *Mon. Wea. Rev.* **111**, 2194-](#)

758 2213.

759 Krishnamurti, T. N., S. Low-Nam, and R. Pasch, 1983: Cumulus parameterizations and rainfall
760 rates II, *Mon. Wea. Rev.*, 111, 815–828.

761 Kubota, P. Y., 2012: Variability of storage energy in the soil-canopy system and its impact on
762 the definition of precipitation standard in South America. Ph.D. Thesis in Portuguese with
763 abstract in English. Instituto Nacional de Pesquisas Espaciais (INPE), São José dos
764 Campos, 285p.

765 Kucharik, C. J., and coauthors, 2000: Testing the performance of a Dynamic Global Ecosystem
766 Model: Water balance, carbon balance, and vegetation structure, *Global Biogeochem.*
767 *Cycles*, **14**, 795-826.

768 [Lima, K. C., P. Satyamurty, and J. P. R. Fernández \(2010\), Largescale atmospheric conditions](#)
769 [associated with heavy rainfall episodes in Southeast Brazil, *Theor. Appl. Climatol.*, **101**,](#)
770 [121–135.](#)

771 Ma, H.-Y., and Coauthors, 2014: On the Correspondence between Mean Forecast Errors and
772 Climate Errors in CMIP5 Models. *J. Climate*, **27**, 1781–1798.

773 [Machenhauer, B., 1977: On the dynamics of gravity oscillations in a shallow water model with](#)
774 [applications to normal mode initialization. *Contrib. Atmos. Phys.* 50, 253-271.](#)

775 [Martin, G. M., D. W. Johnson, and A. Spice, 1994: The measurement and parameterization of](#)
776 [effective radius of droplets in warm stratocumulus clouds. *J. Atmos. Sci.*, **51**, 1823–1842.](#)

777 [Mehran, A., A. Agha Kouchak and T.J. Phillips, 2014: Evaluation of CMIP5 continental](#)
778 [precipitation simulations relative to satellite-based gauge-adjusted observations. *J.*](#)
779 [Geophys. Res., **119**, 1695-1707.](#)

780 Mellor, G. L. and T. Yamada, 1982: Development of a turbulence closure model for geophysical

781 fluid problems. *Rev. Geophys. Space Phys.*, **20**, 851-875.

782 Mesinger, F., and T. L. Black, 1992: On the impact on forecast accuracy of the step-mountain
783 (eta) vs. sigma coordinate. *Meteorol. Atmos. Phys.*, **50**, 47–60.

784 ———, 2008: Bias adjusted precipitation threat scores. *Adv. Geosci.*, **16**, 137–142.

785 Mlawer, E. J., S. J. Taubman, P. D. Brown, M. J. Iacono, and S. A. Clough, 1997: Radiative
786 transfer for inhomogeneous atmospheres: RRTM, a validated correlated-k model for the
787 longwave. *J. Geophys. Res.*, **102**, 16,663-16,682.

788 Morrison, G., J. A. Curry, and V. I. Khvorostyanov, 2005: A new double-moment microphysics
789 parameterization for application in cloud and climate models. Part I: Description, *J. Atmos. Sci.*,
790 **62**, 1665–1677.

791 ———, G. Thompson, and V. Tatarskii, 2009: Impact of Cloud Microphysics on the Development
792 of Trailing Stratiform Precipitation in a Simulated Squall Line: Comparison of One- and
793 Two-Moment Schemes. *Mon. Wea. Rev.*, **137**, 991–1007.

794 Moura, A. D., and J. Shukla, 1981: On the Dynamics of Droughts in Northeast Brazil:
795 Observations, Theory and Numerical Experiments with a General Circulation Model. *J.*
796 *Atmos. Sci.*, **38**, 2653–2675.

797 Murphy, A.H., 1988: Skill Scores Based on the Mean Square Error and Their Relationships to
798 the Correlation Coefficient. *Mon. Wea. Rev.*, **116**, 2417–2424.

799 Neale, R.B, J. Richter, S. Park, P. H. Lauritzen, S. J. Vavrus, P. J. Rasch, and M. Zhang, 2013:
800 The mean climate of the Community Atmosphere Model (CAM4) in forced SST and fully
801 coupled experiments. *J. Climate*, **26**, 5150 –5168

802 Neale, R. B., and coauthor, 2012: Description of the NCAR Community Atmosphere Model
803 (CAM 5.0), *Tech. Note NCAR/TN-486+STR*, NCAR, Boulder, CO.

804 Nobre, P., and J. Shukla, 1996: Variations of Sea Surface Temperature, Wind Stress, and
805 Rainfall over the Tropical Atlantic and South America. *J. Climate.*, **9**, 2464–2479.

806 ———, M. Malagutti, D. F. Urbano, R. A. F. de Almeida and E. Giarolla, 2009: Amazon
807 Deforestation and Climate Change in a Coupled Model Simulation. *J. Climate*, **22**, 5686–
808 5697.

809 ———, and Coauthors, 2013: Climate simulation and change in the Brazilian climate model. *J.*
810 *Climate*, **26**, 6716–6732.

811 Nogués-Peagle, J. and K.C MO, 1997: Alternating wet and dry conditions over South America
812 during summer. *Mon. Wea. Rev.*, **125**, 279–291.

813 Ochoa A., L. Pineda, P. Willems, and P. Crespo, 2014: Evaluation of TRMM 3B42 (TMPA)
814 precipitation estimates and WRF retrospective precipitation simulation over the Pacific-
815 Andean basin into Ecuador and Peru. *Hydrol. Earth Syst. Sci*, **11**, 411–449.

816 Panetta, J.; S. R. Barros, J. P. Bonatti, S. S. Tomita and P. Y. Kubota, 2007: Computational Cost
817 of CPTEC AGCM. Computational cost of CPTEC AGCM. Proceedings of the 12th
818 Workshop on Use of high performance computing in meteorology. Reading, 65-83.

819 Park, S. and C. S. Bretherton, 2009: The University of Washington Shallow Convection and
820 Moist Turbulence Schemes and Their Impact on Climate Simulations with the Community
821 Atmosphere Model. *J. Climate*, **22**, 3449–3469.

822 Pincus, R., H. W. Barker, and J-J Morcrette, 2003: A fast, flexible, approximate technique for
823 computing radiative transfer in inhomogeneous cloud fields. *J. Geophys. Res.*, **108**, D13.

824 Rasmussen, K. L., and R. A. Houze Jr., 2016: Convective initiation near the Andes in subtropical
825 South America. *Mon. Wea. Rev.*, **144**, 2351–2374, doi:10.1175/MWR-D-15-0058.1.

826

827 ———, M. M. Chaplin, M. D. Zuluaga⁺, and R. A. Houze, Jr., 2016: Contribution of Extreme
828 Convective Storms to Rainfall in South America. *J. Hydrometeor.*, **17**, 353-367.

829 Rasch, P.J. and J.E. Kristjansson, 1998: A comparison of the CCM3 model climate using
830 diagnosed and predicted condensate parameterizations, *J. Climate.*, **11** 1587 - 1614

831 Reisner, J., R. M. Rasmussen, and R. T. Bruintjes, 1998: Explicit forecasting of supercooled
832 liquid water in winter storms using the MM5 mesoscale model. *Quart. J. Roy. Meteorol.*
833 *Soc.*, **124**, 1071–1107.

834 Romatschke, U., and R. A. Houze Jr., 2010: Extreme summer convection in South America. *J.*
835 *Climate*, **23**, 3761–3791.

836 Rozante, J.R. and I.F.A. Cavalcanti, 2008: Regional Eta model experiments. SALLJEX and
837 MCS development. *J. Geophys. Res.*, **113**, D17106, doi: 10.1029/2007JD009566.

838 Salio P., M. Nicolini, and E.J. Zipser, 2007: Mesoscale Convective Systems over Southeastern
839 South America and Their Relationship with the South American Low-Level Jet. *Mon. Wea.*
840 *Rev.*, **135**, 1290–1309.

841 Sato, N., P. J. Sellers, D. A. Randall, E. K. Schneider, J. Shukla, J. L. Kinter III, Y. T. Hou, and
842 E. Albertazzi, 1989: Effects of implementing the Simple Biosphere Model in a general
843 circulation model. *J. Atmos. Sci.*, **46**, 2757–2782.

844 Siqueira, J. R. and V. S. Marques, 2010. Structural characteristics of mesoscale convective
845 systems over southeast Brazil related to cold frontal and non-frontal incursions.
846 *Australian Meteorological and Oceanographic Journal*, **60**, 49-62.

847 Stern, H., 2008: The accuracy of forecasts for Melbourne, Australia. *Meteorol. Appl.* **15**: 65–71.

848 Stern, H., and N. E., Davidson, 2015: Trend in the skill of weather prediction at lead-times of 1-
849 14 days. *Quart. J. Roy. Meteorol. Soc.*, **141**, 2726–2736.

850 [Tarasova, T., and B. Fomin, 2000: Solar radiation absorption due to water vapor: Advanced](#)
851 [broadband parameterizations. *J. Appl. Meteor.*, **39**, 1947-1951.](#)

852 [Taylor, K. E., 2001: Summarizing multiple aspects of model performance in a single diagram. *J.*](#)
853 [Geophys. Res.](#), **106**, 7183-7192.

854 Vera, C., W. Higgins, J. Amador, T. Ambrizzi, R. Garreaud, D. Gochis, D. Gutzler, D.
855 Lettenmaier, J. Marengo, C. R. Mechoso, J. Noguez-Paegle, P. L. Silva Dias, and C.
856 Zhang, 2006: Toward a Unified View of the American Monsoon Systems. *J. Climate*, **19**,
857 4977–5000.

858 Vieira, S. O., P. Satyamurty, and R.V. Andreoli, 2012: On the South Atlantic Convergence
859 Zone affecting southern Amazonia in austral summer. *Atmosph. Sci. Lett.*, 14: 1–6.
860 doi: 10.1002/asl2.401

861 [Webster S., A. R. Brown, D. R. Cameron, and C. P. Jones, 2003: Improvements to the](#)
862 [representation of orography in the Met Office United Model. *Q. J. R. Meteorol. Soc.*, **129**,](#)
863 [1989–2010.](#)

864 WMO, 2009: Recommendations for the Verification and Intercomparison of QPFs and PQPFs
865 from Operational NWP Models - Revision 2 October 2008 (WMO/TD-No.1485 WWRP
866 2009-1). Available online at:
867 http://www.wmo.int/pages/prog/arep/wwrp/new/documents/WWRP2009-1_web_CD.pdf.

868 Xie, S., H.-Y Ma, J. S. Boyle, S.A. Klein, and Y. Zhang, 2012: On the Correspondence between
869 Short- and Long-Time-Scale Systematic Errors in CAM4/CAM5 for the Year of Tropical
870 Convection. *J. Climate*, **25**, 7937–7955.

871 [Xue, Y., P. J. Sellers, J. L. Kinter, and J. Shukla, 1991: A simplified biospheremodel for global](#)
872 [climate studies. *J. Climate*, **4**, 345–364.](#)

873 [Yin L., F. Fu, E. Shevliakova and R. E. Dickinson, 2013: How well can CMIP5 simulate](#)
874 [precipitation and its controlling processes over tropical South America? *Clim. Dyn.*,](#)
875 [41,3127–3143.](#)

876 [Zeng, X., M. Zhao, and R.E. Dickinson, 1998: Intercomparison of bulk aerodynamical](#)
877 [algorithms for the computation of sea surface fluxes using TOGA COARE and TAO data.](#)
878 [*J. Climate*, 11, 2628-2644.](#)

879 Zhang, G. J., 2002: Convective quasi-equilibrium in midlatitude continental environment and its
880 effect on convective parameterization. *J. Geophys. Res.*, 107 (D14),
881 doi:10.1029/2001JD001005.

882 ———, 2009: Effects of entrainment on convective available potential energy and closure
883 assumptions in convection parameterization. *J. Geophys. Res.*, 114, D07109,
884 doi:10.1029/2008JD10976.

885 Zhu, H., M. C. Wheeler, A. H. Sobel, and D. Hudson, 2014: Seamless Precipitation Prediction
886 Skill in the Tropics and Extratropics from a Global Model. *Mon. Wea. Rev.*, 142, 1556–
887 1569.

888 **LIST OF TABLES**

889 **Table 1.** Summary of the dynamic and physics configurations in AGCM3 and BAM.

890 **Table 2.** Experiments description.

891 **Table A1.** Brief overview of mass fluxes and parameters used in the GDM ensemble scheme. In
892 this scheme 6 different closures (3 perturbations for Grell closure and 3 perturbations for CAPE-
893 based closure) from the dynamic control are allowed to interact with 9 members from the static
894 control (3 efficiencies and 3 cap strengths), giving a total of 54 sub-grid members.

895

896

897

898

899

Table 1. Summary of the dynamic and physics configurations in AGCM3 and BAM

<i>Dynamics and Physics</i>	<i>CPTEC/AGCM3 (old)</i>	<i>CPTEC/BAM (new)</i>
Dynamics	<i>Spectral Eulerian or semi-Lagrangian semi-implicit model, with hydrostatic approximation, sigma vertical coordinates, full or reduced gaussian grids, fully parallel (MPI + OPenMP)</i>	<i>Spectral Eulerian or semi-Lagrangian semi-Implicit model, with hydrostatic approximation, sigma/hybrid vertical coordinates, full or reduced gaussian grids, semi-Lagrangian monotonic transport scheme (on the model grid) of moisture, microphysics prognostic variables and tracers, fully parallel (MPI + OPenMP)</i>
Land surface process	<i>Simplified Simple Biosphere (SSiB) scheme, Xue et al. (1991)</i>	<i>Dynamic vegetation model, the Integrated Biosphere Simulator -IBIS (Foley et al. 1996 and Kucharik et al. 2000), implemented, adapted and improved by Kubota (2012)</i>
Sea-air surface fluxes	<i>The bulk transfer coefficients are determined by analytical functions (Sato et al. 1989)</i>	<i>The bulk transfer coefficients are determined by using the Monin–Obukhov theory and the Tropical Oceans Global Atmosphere (TOGA) Coupled Ocean–Atmosphere Response Experiment (COARE) data (Zeng et al. 1998)</i>
Vertical diffusion	<i>Local Mellor-Yamada (1982), coupled to SSiB equations</i>	<i>Modified the Mellor-Yamada (1982) scheme by adding the counter-gradient adjustment term to the eddy diffusion equation</i>
Gravity-wave Drag	<i>Alpert et al. (1988) scheme without low-level blocking</i>	<i>Webster et al. (2003) scheme with low-level blocking</i>
Cloud microphysics	<i>Single-moment Microphysics scheme (Rasch and Kristjansson, 1998)</i>	<i>Double-moment Microphysics scheme (Morrison et al. 2009)</i>
Radiation Short and long-wave	<i>CLIRAD, Chou and Suarez (1999) and modified by Tarasova and Fomin (2000)</i>	<i>RRTMG, Iacono et al. (2008, developed at Atmospheric and Environmental Research, Inc. (AER)</i>

Shallow Convection	<i>Tiedtke (1983) diffusion scheme</i>	<i>University of Washington (UW) Shallow convection (Park and Bretherton, 2009)</i>
Deep Convection	<i>Grell and Dévényi (2002) ensemble scheme (GD)</i>	<i>-Grell and Dévényi (2002) ensemble scheme (GD) -Modified the GD scheme (GDM), described briefly in this paper (Appendix).</i>

901

902

903

904

905

Table 2. Experiments description.

<i>Exp.</i>	<i>Quadratic grid horizontal resolution with a reduced Gaussian grid</i>	<i>Time Step (s)</i>	<i>Dynamics: Model version- Eulerian (EU) or semi_Lagrangian (SL)</i>	<i>Physics: Model version, Except deep convection</i>	<i>Deep Convection</i>	<i>Model version-dynamics-resolution</i>
Exp 1	T_{Q299} ($0.4^\circ \approx 45$ km)	240	AGCM3-EU	AGCM3	GD	AGCM3-EU-45 km
Exp 2	T_{Q299} ($0.4^\circ \approx 45$ km)	240	BAMa-EU	BAMa	GD	BAMa-EU-45 km
Exp 3	T_{Q299} ($0.4^\circ \approx 45$ km)	240	BAMb-EU	BAMb	GDM	BAMb-EU-45 km
Exp 4	T_{Q666} ($0.18^\circ \approx 20$ km)	400	BAMb-SL	BAMb	GDM	BAMb-SL-20 km

906

907

908

909

910

911 Table A1. Brief overview of mass fluxes and parameters used in the GDM ensemble scheme. In
 912 this scheme 6 different closures (3 perturbations for Grell closure and 3 perturbations for CAPE-
 913 based closure) from the dynamic control are allowed to interact with 9 members from the static
 914 control (3 efficiencies and 3 cap strengths), giving a total of 54 sub-grid members.

<i>Dynamic and Static control</i>	<i>Definition of the type of Closures in dynamic control and parameters in static control</i>	<i>Number of variations</i>	<i>Mass flux (dynamic control) or parameters (static control)</i>
Dynamic control	Grell closure: Assume AS quasi-equilibrium between large-scale forcing (<i>LS</i>) and convection (Grell, 1993).	3	$m_b = -\frac{1}{K} \left(\frac{\partial A}{\partial t} \right)_{LS}$ $A = \int_{z_b}^{z_t} \eta(z) B(z) dz$
Dynamic control	CAPE-based closure: Assumes that quasi-equilibrium exists between convection and the large-scale process in the free troposphere (Zhang 2002 and Zhang 2009). Note, $CAPE_{env}$ is similar to the work function definition, but without weighing by a normalized mass flux profile (η), and the buoyancy force B can be calculated with and without dilution.	3	$m_b = -\frac{1}{K} \left(\frac{\partial CAPE_{env}}{\partial t} \right)_{LS}$ $CAPE_{env} = \int_{z_b}^{z_t} B(z) dz$
Static control feedback	Precipitation efficiency (f) perturbations. The convective rainfall (R) is defined as a function of precipitation efficiency (f), integrated condensate in the updraft (I), which depends on the total water that is rained out (S_u) and m_a (Grell and Dévényi, 2002).	3	$R = f I m_a$, $I(\lambda) = \int_{z_b}^{z_t} n_u(\lambda, z) S_u dz$ $f = (0.25, 0.5, 0.75)$
Static control feedback	Maximum depth of capping ($CapMax$) perturbations. The scheme does not allow convection until the lifting required for parcels to reach their level of free convection becomes less than specified $CapMax$ ($25 mb < CapMax > 25 mb$)	3	$CapMax = (60, 90, 120)$

915

916

917

918

919

920 **LIST OF FIGURES**

921 **Fig. 1.** Precipitation (left) and surface latent heat fluxes (right) averaged over DJF 2012-2013
922 from GPCP (a), Era-Interim reanalysis (a'), and the 24 h forecast of the models. Old model
923 AGCM3 (Exp1) (b, b'), new model BAMa (Exp2) (c, c') and new model BAMb with GDM
924 convective scheme (Exp3) (d-d'). Model identifications are indicated in the bottom-left corner of
925 the panels; while spatially-averaged *RMSE* and correlation coefficient (*CORR*) are given in the
926 top-right corner of the panels. Boxes defined in (a) indicate approximately the regions with
927 intense precipitation during DJF over Southern Hemisphere. Africa (1), Indian Ocean ITCZ (2),
928 South Pacific Convergence Zone (SPCZ, 3), Amazon Basin (4), South Atlantic Convergence
929 Zone (SACZ, 5), and La Plata Basin (6).

930 **Fig. 2.** Zonal mean precipitation (a) and surface latent heat fluxes (b) corresponding to Fig. 1 for
931 24 h forecasts by different models indicated in the panels.

932 **Fig. 3.** Mean precipitation averaged over DJF 2012-2013 from TMPA-3B4 (a) and from three
933 NWP model 24 h forecasts and their differences from TMPA respectively BAMb (Exp3) at 45
934 km (b, b'), BAMb at 20 km (Exp4) (c, c') and GFS at 27 km (d, d'). Rectangular boxes A1, A2,
935 A3, A4 and A5 in panel (a) are the regions used for the comparison of results: Global Tropics
936 (30° S - 30° N), Africa, Australia, South Pacific Convergence Zone (SPCZ), and South America,
937 respectively.

938 **Fig. 4.** Daily mean precipitation for the period 01 December 2012 to 28 February 2013 from 24
939 h (left) and 72 h (right) forecasts for the areas defined in Fig.3a from TMPA and three NWP
940 models indicated in the panel.

941 **Fig. 5.** The performance of the models BAMa (Exp2), BAMb (Exp3 and Exp4) and GFS in
942 terms of precipitation mean bias (BIAS), and unbiased RMSE (URMSE) for the areas defined in

943 Fig.3a.

944 **Fig. 6.** Frequency Bias (left panel) and Gilbert Skill Score (right panel) as function of
945 precipitation threshold for the areas defined in Fig. 3a, with 72 hours in advance by models
946 indicated in the panel.

947 **Fig. 7.** Taylor diagrams comparing the precipitation simulation statistics, correlation coefficient,
948 unbiased RMSE normalized (URMSE*), and standard deviation normalized from the models for
949 the areas defined in Fig.3a. The black star indicates perfect agreement. The numbers in the
950 diagram indicate forecast range in days.

951 **Fig. 8.** Map of South America with the geographic regions of Brazil (shaded). Boxes B1 to B5
952 are considered for model evaluation. B1 represents approximately La Plata Basin (which
953 includes Southern Brazil, Northeast Argentina, Southern Paraguay and Uruguay). The boxes B2,
954 B3, B4 and B5 represent approximately the Southeast, Central West, Northeast and North
955 regions of Brazil. B5 also represents approximately the Brazilian Amazon Basin (referred to as
956 Amazon).

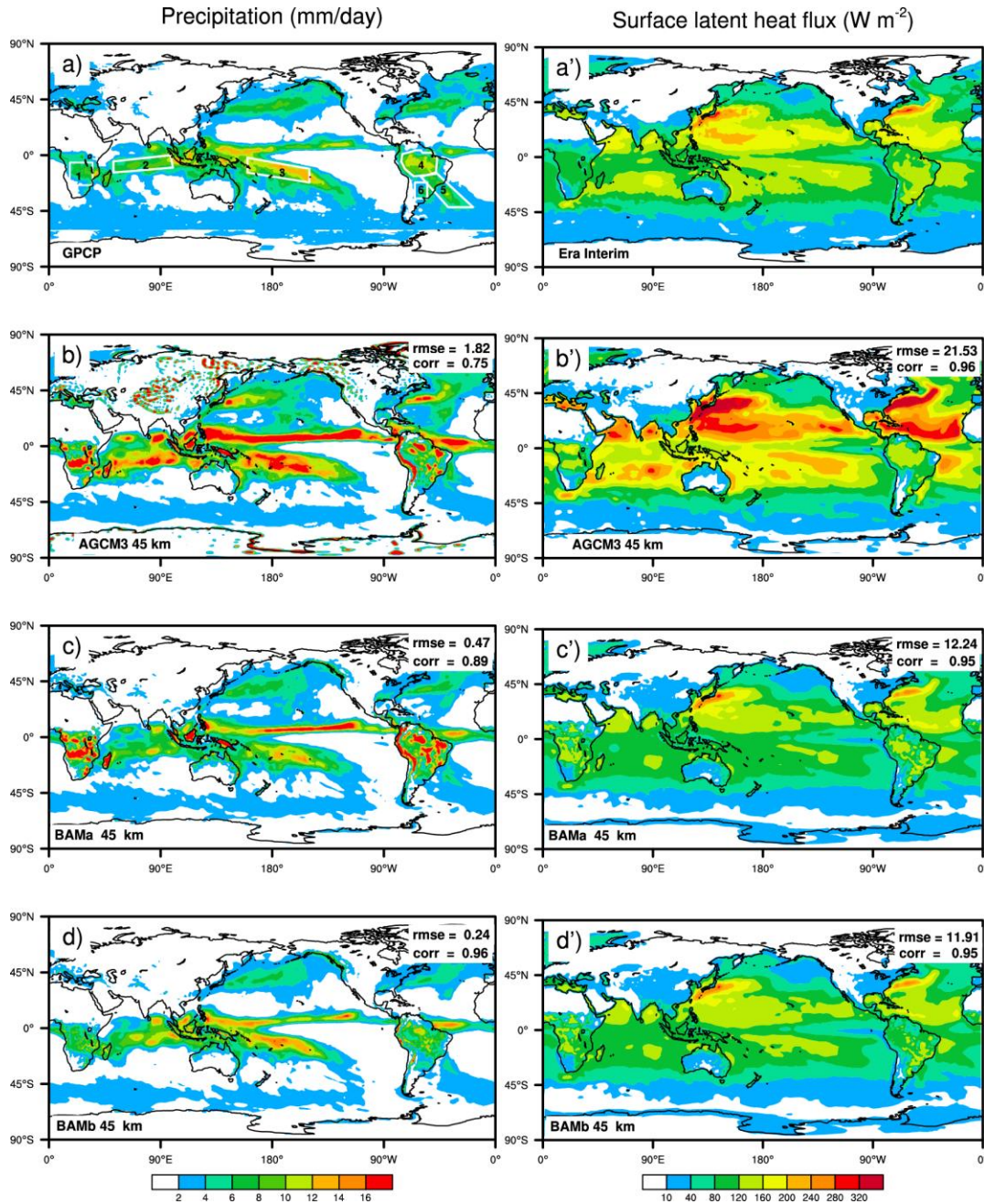
957 **Fig. 9.** Daily mean precipitation for the period 01 December 2012 to 28 February 2013 from 24
958 h (left) and 72 h (right) forecasts for the areas defined in Fig. 8 from TMPA and three NWP
959 models indicated in the panel. The letters F in (a) and S in (b) indicate cold fronts over La Plata
960 and SACZ events over Southeast respectively.

961 **Fig. 10.** As Figure 5, except for the areas defined in Fig. 8.

962 **Fig. 11.** Same as in Fig. 6, except for the areas defined in Fig. 8.

963 **Fig. 12.** Same as in Fig. 7, except for the areas defined in Fig. 8.

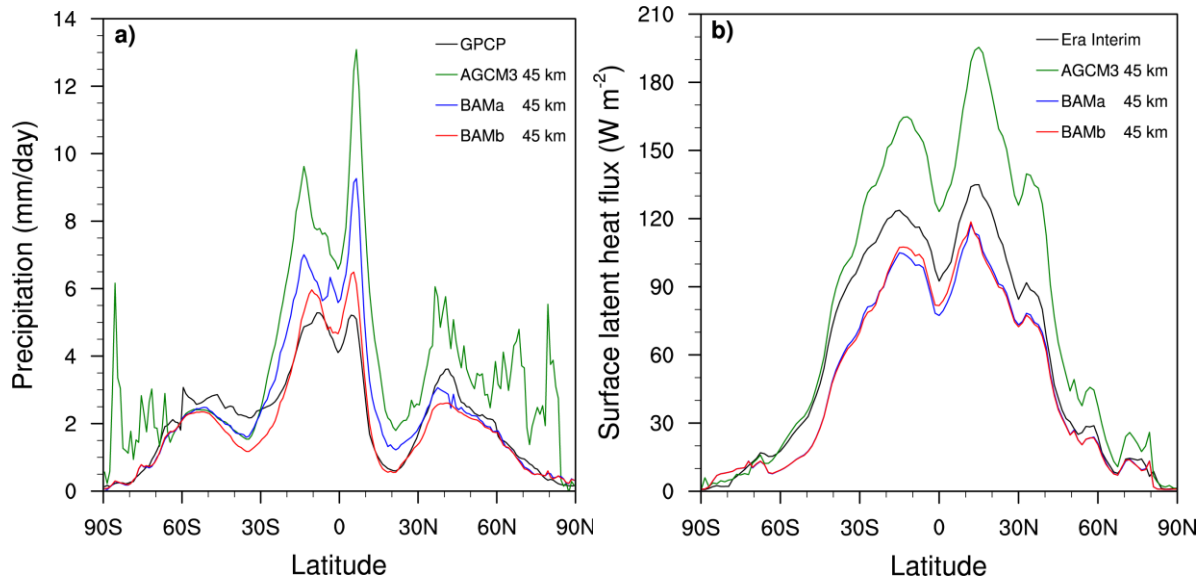
964



965

966 Fig. 1. Precipitation (left) and surface latent heat fluxes (right) averaged over DJF 2012-2013
 967 from GPCP (a), Era-Interim reanalysis (a'), and the 24 h forecast of the models. Old model
 968 AGCM3 (Exp1) (b, b'), new model BAMA (Exp2) (c, c') and new model BAMb with GDM
 969 convective scheme (Exp3) (d-d'). Model identifications are indicated in the bottom-left corner of
 970 the panels; while spatially-averaged *RMSE* and correlation coefficient (*CORR*) are given in the
 971 top-right corner of the panels. Boxes defined in (a) indicate approximately the regions with
 972 intense precipitation during DJF over Southern Hemisphere. Africa (1), Indian Ocean ITCZ (2),
 973 South Pacific Convergence Zone (SPCZ, 3), Amazon Basin (4), South Atlantic Convergence
 974 Zone (SACZ, 5), and La Plata Basin (6).

975



976

977 Fig. 2. Zonal mean precipitation (a) and surface latent heat fluxes (b) corresponding to Fig. 1 for
978 24 h forecasts by different models indicated in the panels.

979

980

981

982

983

984

985

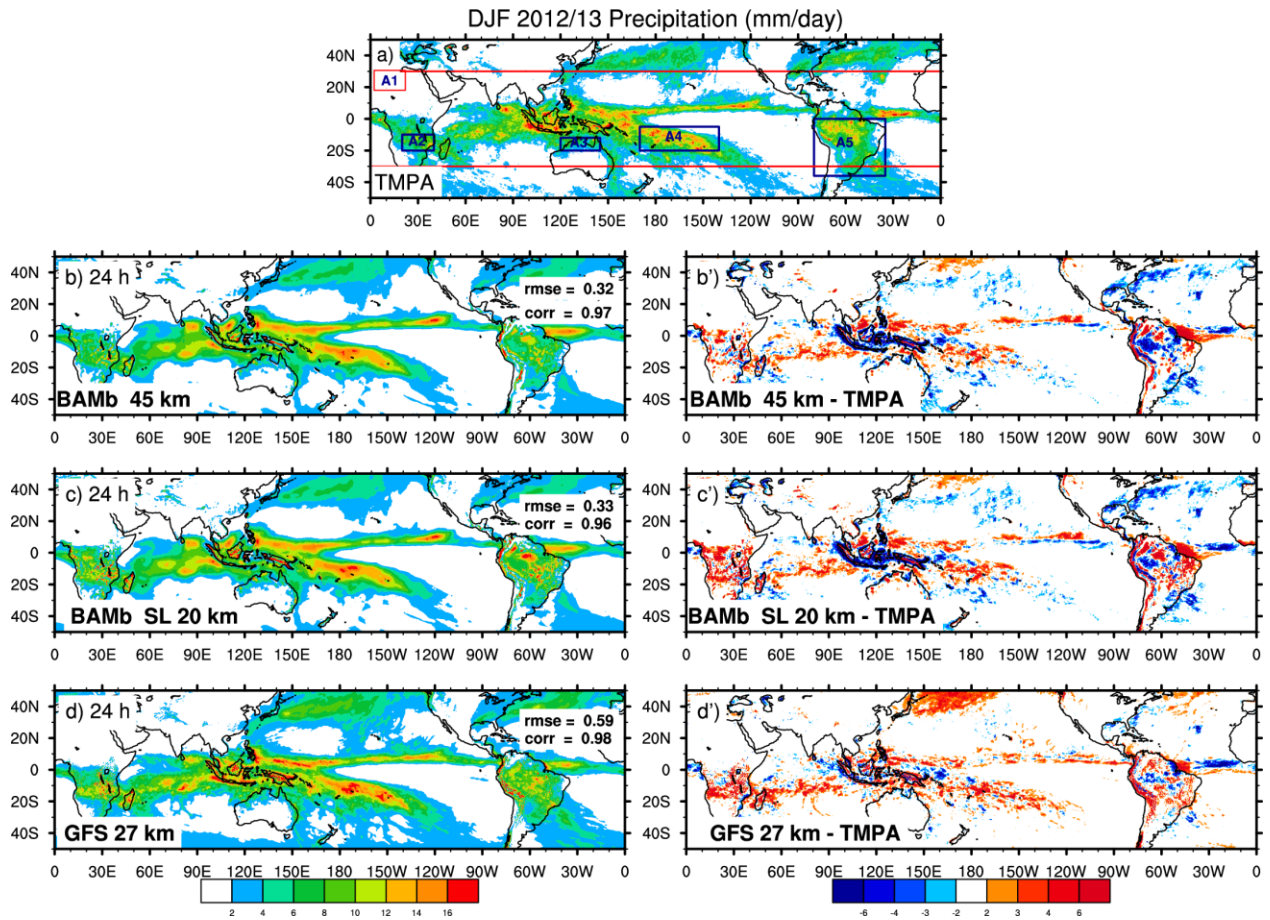
986

987

988

989

990

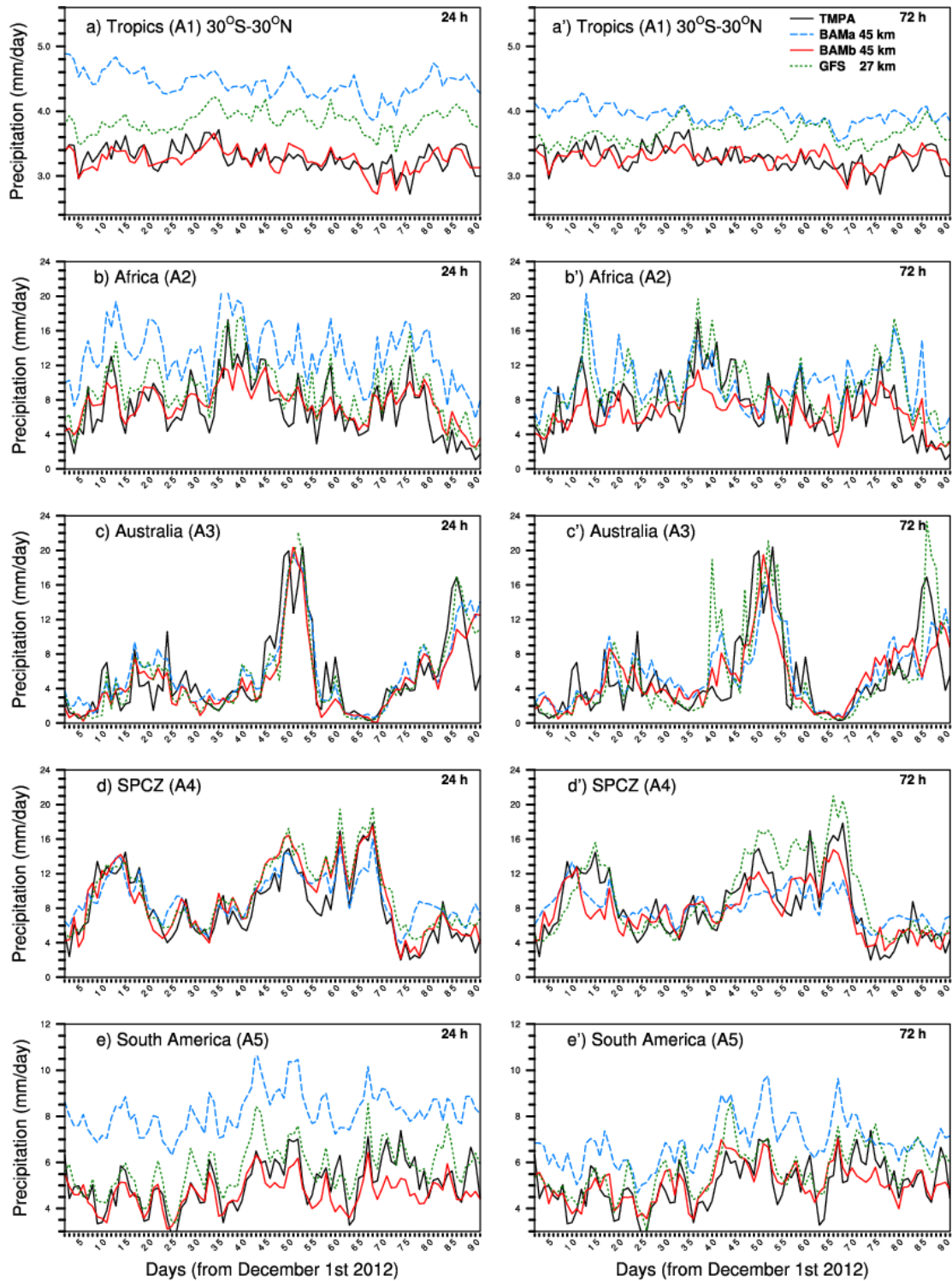


991

992 Fig. 3. Mean precipitation averaged over DJF 2012-2013 from TMPA-3B4 (a) and from three
 993 NWP model 24 h forecasts and their differences from TMPA respectively BAMB (Exp3) at 45
 994 km (b, b'), BAMB at 20 km (Exp4) (c, c') and GFS at 27 km (d, d'). Rectangular boxes A1, A2,
 995 A3, A4 and A5 in panel (a) are the regions used for the comparison of results: Global Tropics
 996 (30° S - 30° N), Africa, Australia, South Pacific Convergence Zone (SPCZ), and South America,
 997 respectively.

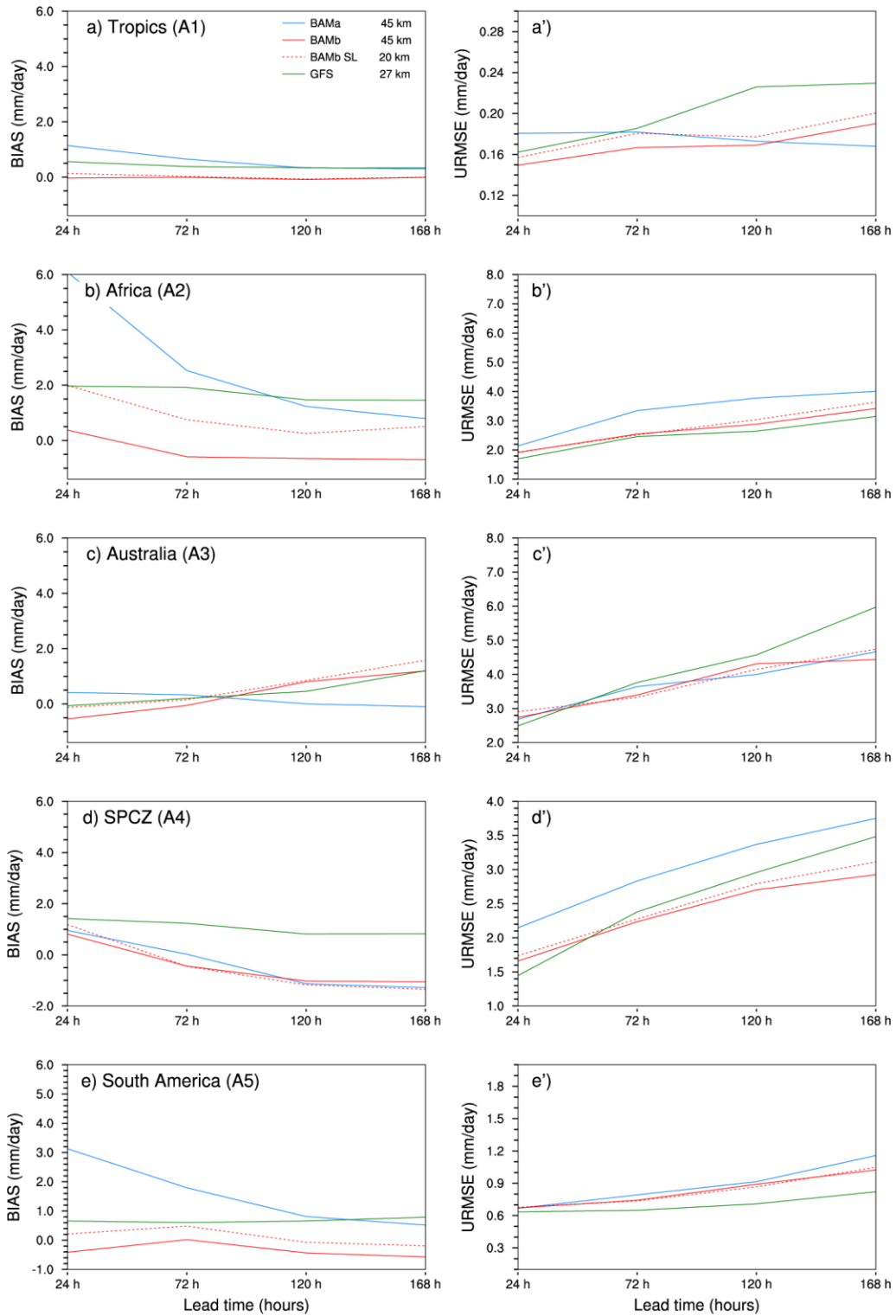
998

999



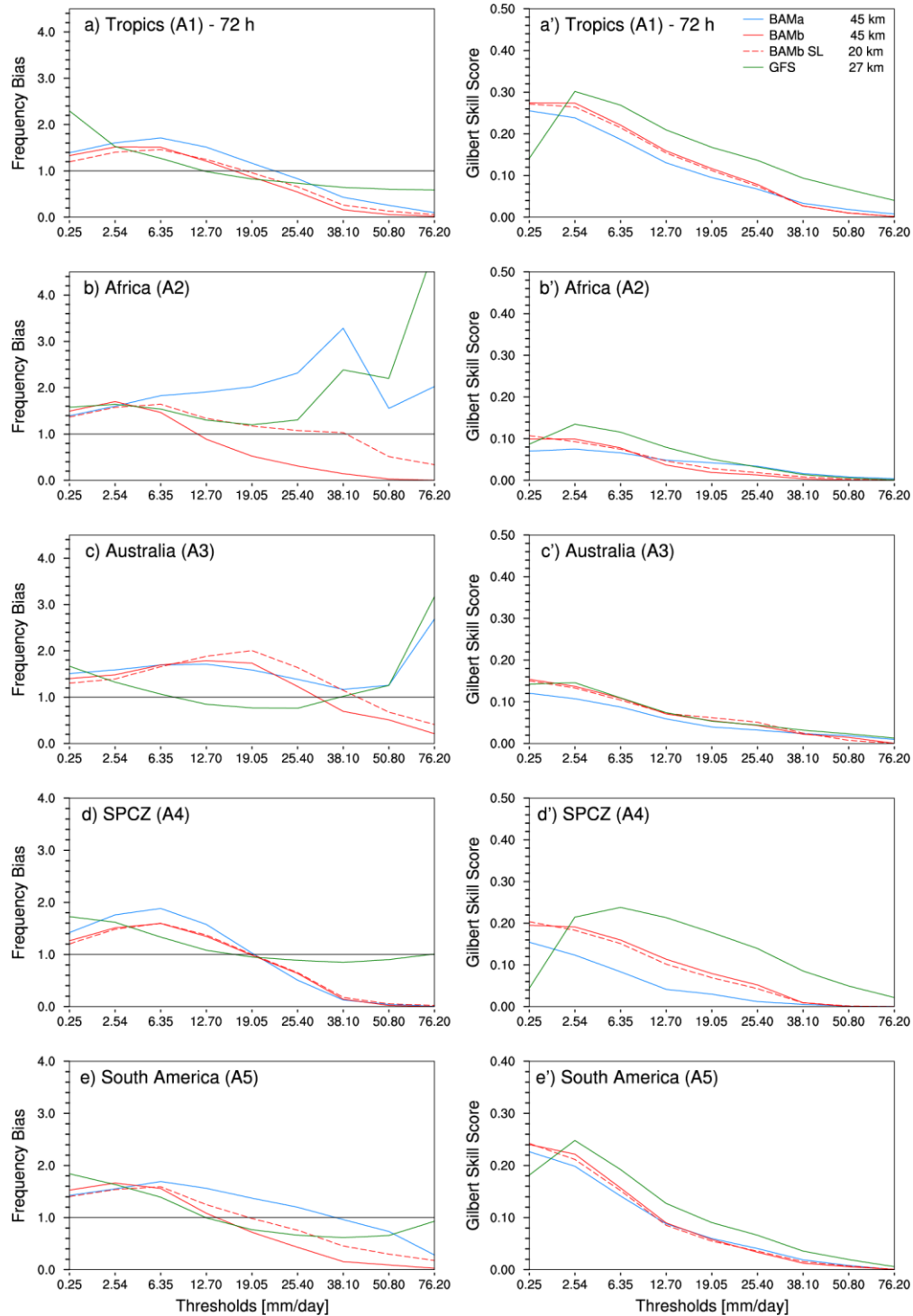
1000

1001 Fig. 4. Daily mean precipitation for the period 01 December 2012 to 28 February 2013 from 24
 1002 h (left) and 72 h (right) forecasts for the areas defined in Fig.3a from TMPA and three NWP
 1003 models indicated in the panel.



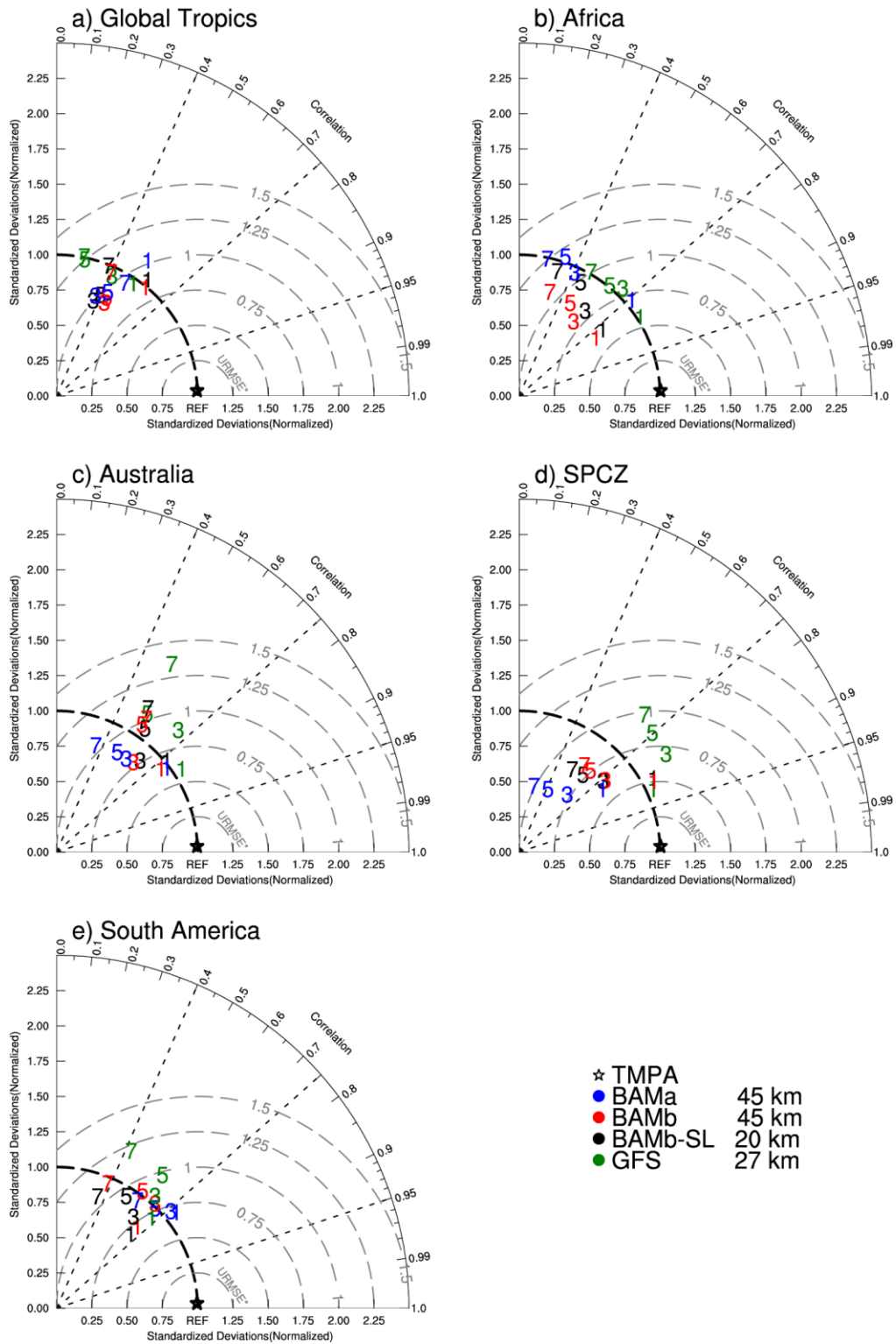
1004

1005 Fig. 5. The performance of the models BAMA (Exp2), BAMB (Exp3 and Exp4) and GFS in
 1006 terms of precipitation mean bias (BIAS), and unbiased RMSE (URMSE) for the areas defined in
 1007 Fig.3a.



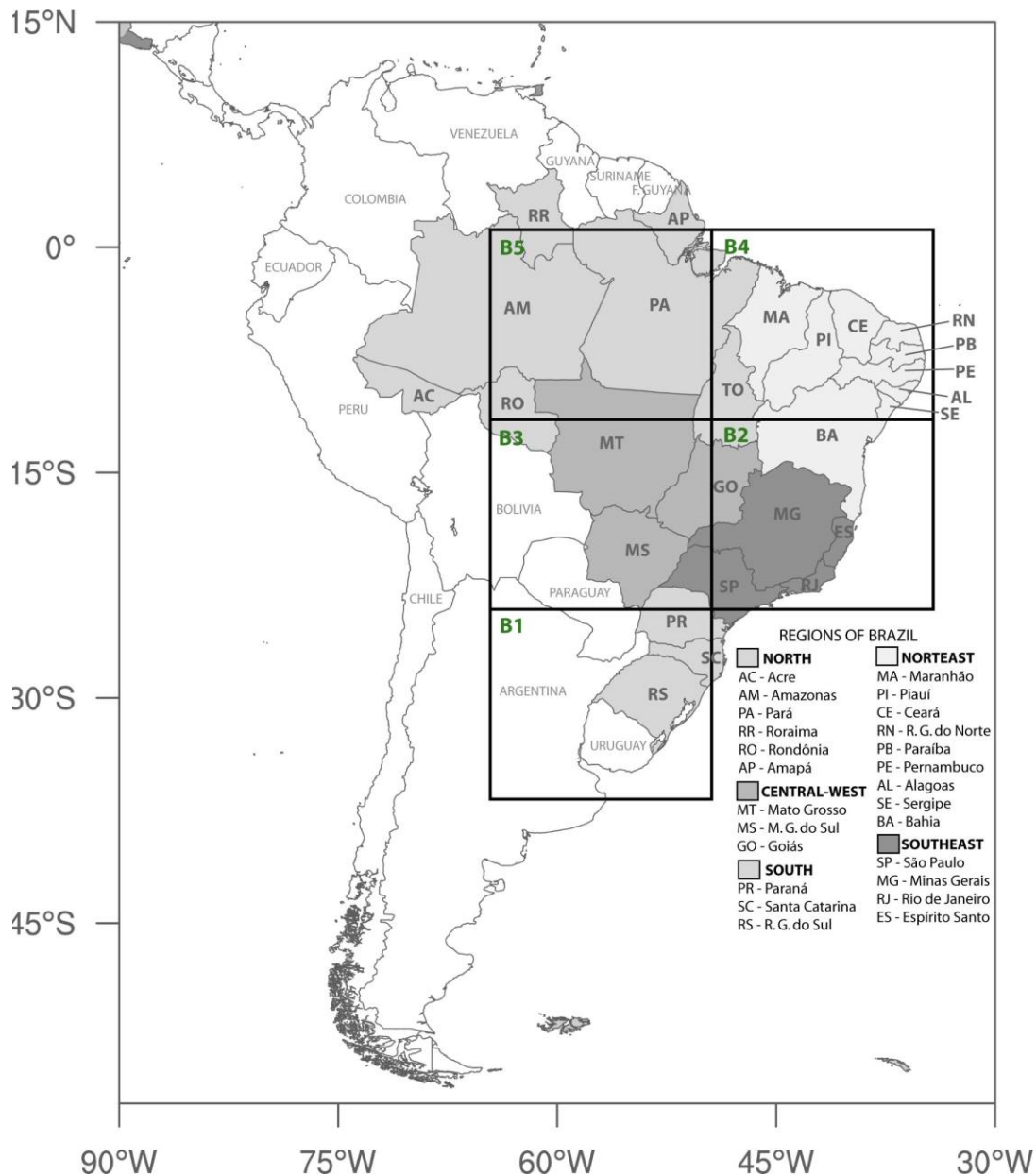
1009

1010 Fig. 6. Frequency Bias (left panel) and Gilbert Skill Score (right panel) as function of
 1011 precipitation threshold for the areas defined in Fig. 3a, with 72 hours in advance by models
 1012 indicated in the panel.



1013

1014 Fig. 7. Taylor diagrams comparing the precipitation simulation statistics, correlation coefficient,
 1015 unbiased RMSE normalized (URMSE*), and standard deviation normalized from the models for the areas defined in Fig.3a. The black star indicates perfect agreement. The numbers in the
 1016 diagram indicate forecast range in days.
 1017

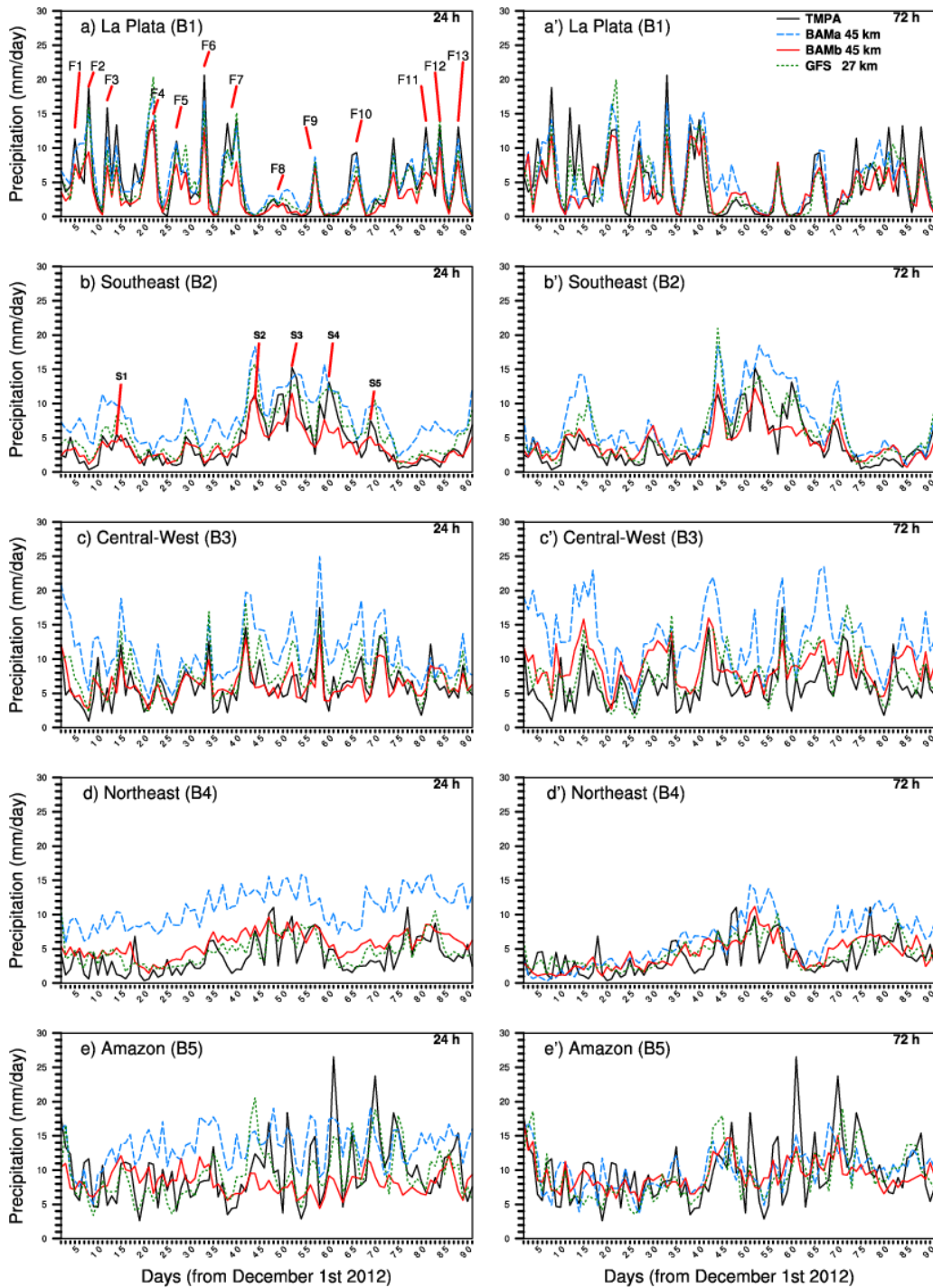


1018

1019

1020 Fig. 8. Map of South America with the geographic regions of Brazil (shaded). Boxes B1 to B5
 1021 are considered for model evaluation. B1 represents approximately La Plata Basin (which
 1022 includes Southern Brazil, Northeast Argentina, Southern Paraguay and Uruguay). The boxes B2,
 1023 B3, B4 and B5 represent approximately the Southeast, Central West, Northeast and North
 1024 regions of Brazil. B5 also represents approximately the Brazilian Amazon Basin (referred to as
 1025 Amazon).

1026



1028

1029 Fig. 9. Daily mean precipitation for the period 01 December 2012 to 28 February 2013 from 24
 1030 h (left) and 72 h (right) forecasts for the areas defined in Fig. 8 from TMPA and three NWP
 1031 models indicated in the panel. The letters F in (a) and S in (b) indicate cold fronts over La Plata
 1032 and SACZ events over Southeast respectively.

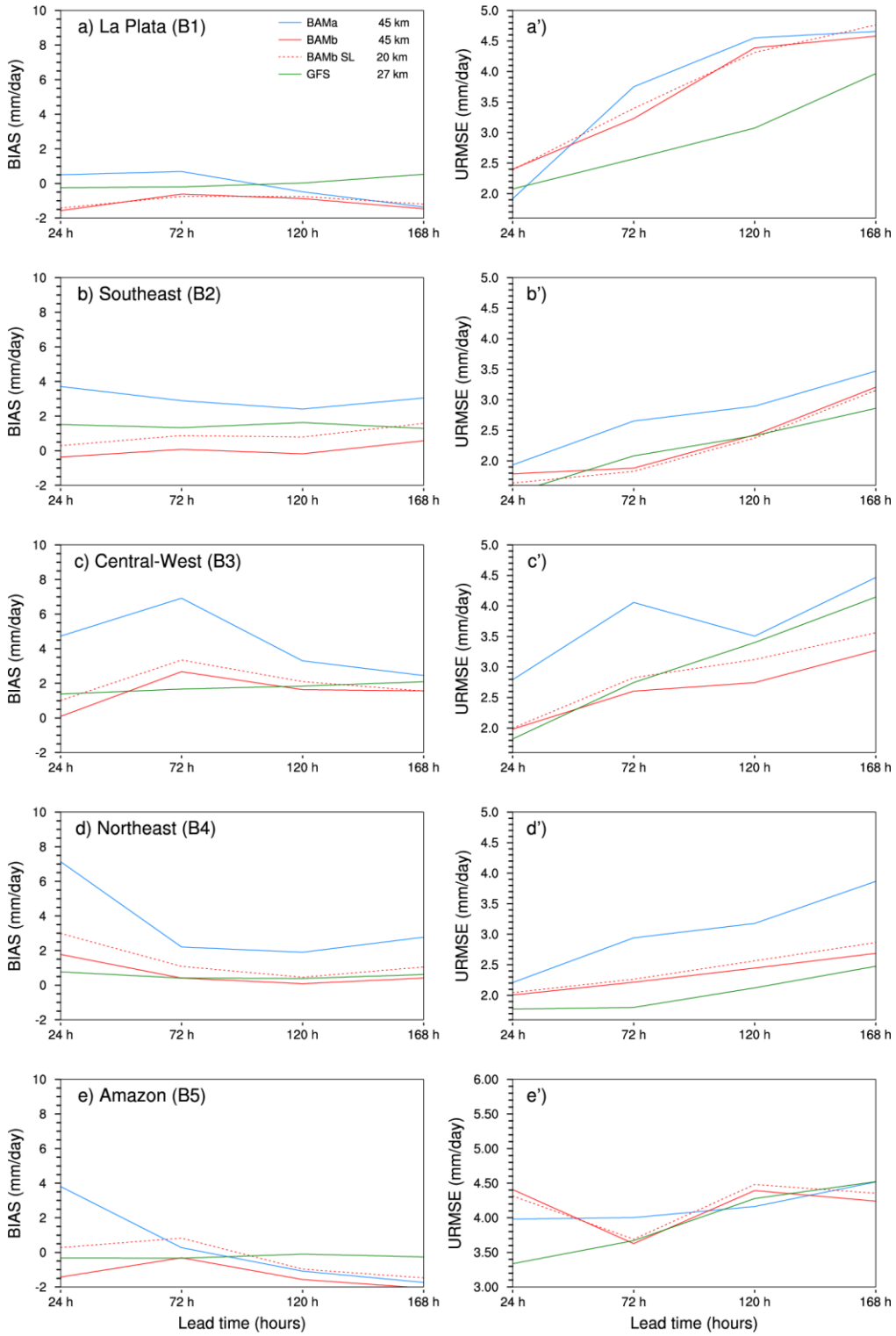
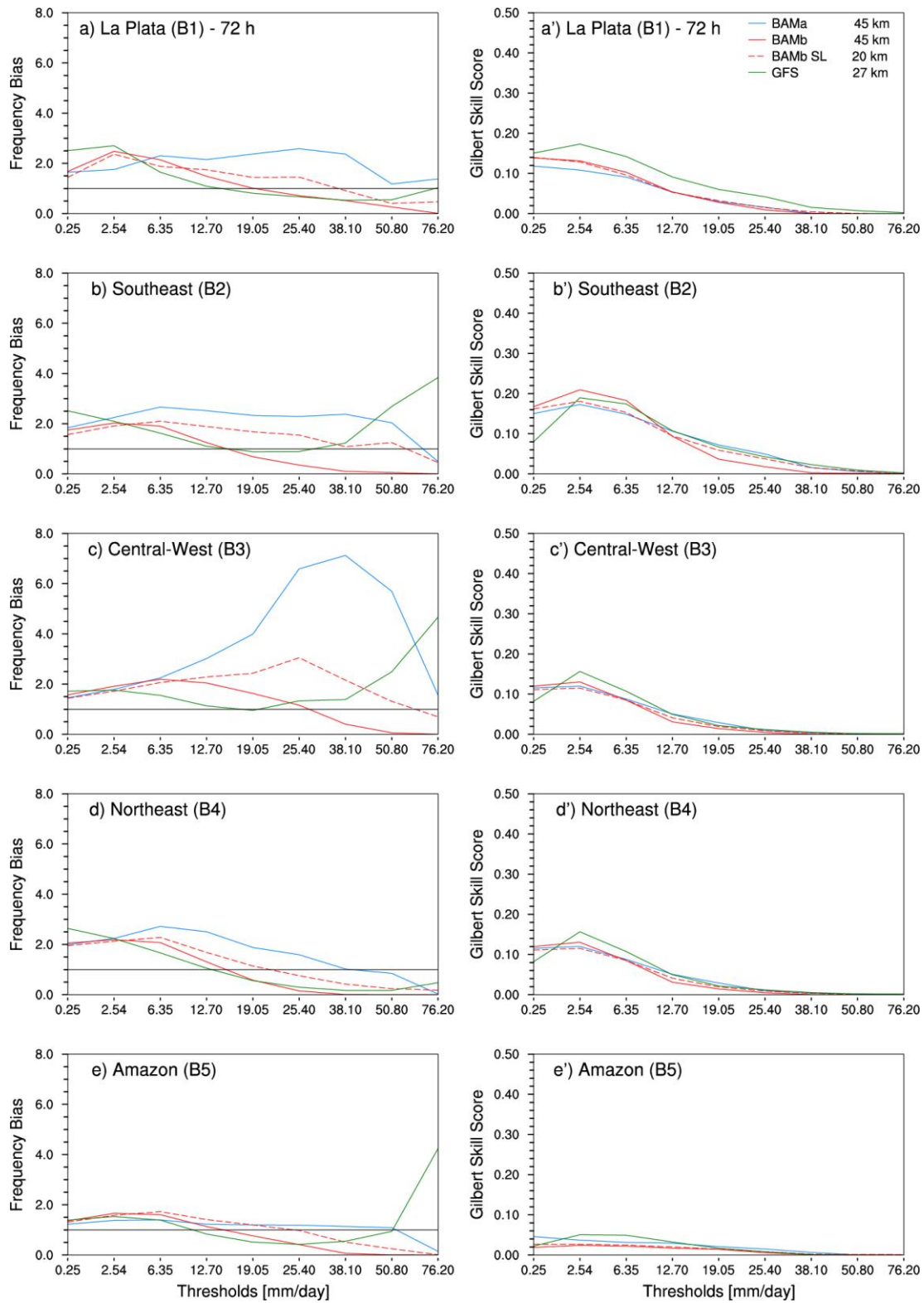


Fig. 10. As Figure 5, except for the areas defined in Fig. 8.

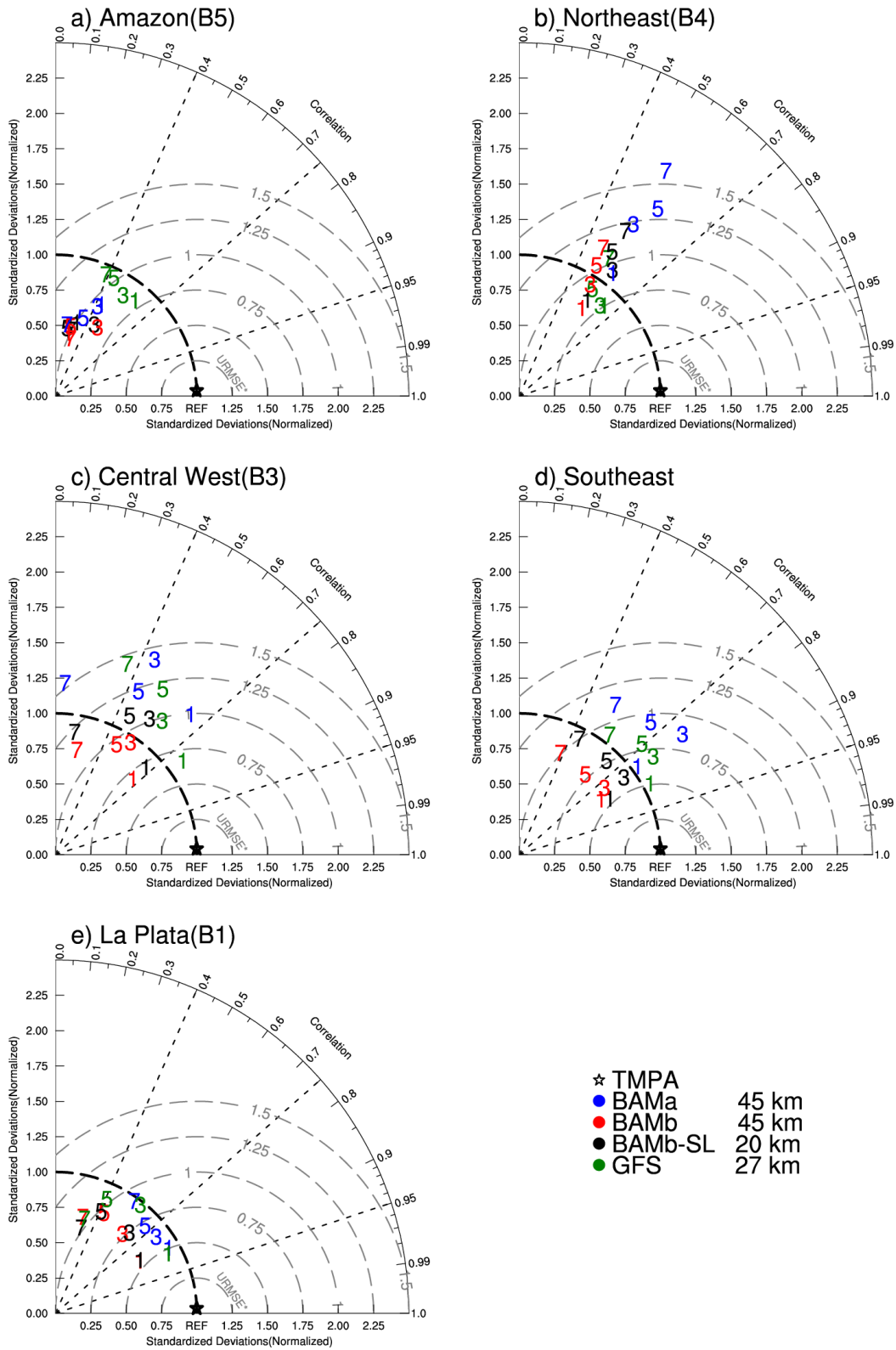


1037

1038

1039

Fig. 11. Same as in Fig. 6, except for the areas defined in Fig. 8.



1040

1041

1042

Fig. 12. Same as in Fig. 7, except for the areas defined in Fig.8.